

Anisotropic magnetism and electronic structure of trigonal EuAl_2Ge_2 single crystals

Santanu Pakhira^{1,*}, Asish K. Kundu,² Farhan Islam,^{1,3} M. A. Tanatar^{1,3}, Tufan Roy⁴, Thomas Heitmann,⁵ T. Yilmaz,⁶ E. Vescovo,⁶ Masahito Tsujikawa⁷, Masafumi Shirai^{4,7}, R. Prozorov,^{1,3} David Vaknin^{1,3} and D. C. Johnston^{1,3}

¹Ames National Laboratory, Iowa State University, Ames, Iowa 50011, USA

²Condensed Matter Physics and Materials Science Division, Brookhaven National Laboratory, Upton, New York 11973, USA

³Department of Physics and Astronomy, Iowa State University, Ames, Iowa 50011, USA

⁴Center for Science and Innovation in Spintronics, Core Research Cluster, Tohoku University, Sendai 980-8577, Japan

⁵The Missouri Research Reactor and Department of Physics and Astronomy, University of Missouri, Columbia, Missouri 65211, USA

⁶National Synchrotron Light Source II, Brookhaven National Laboratory, Upton, New York 11973, USA

⁷Research Institute of Electrical Communication, Tohoku University, Sendai 980-8577, Japan



(Received 23 January 2023; revised 22 March 2023; accepted 18 April 2023; published 28 April 2023)

Understanding the interplay between magnetic and electronic degrees of freedom is of profound recent interest in different Eu-based magnetic topological materials. In this paper, we studied the magnetic and electronic properties of the layered Zintl-phase compound EuAl_2Ge_2 crystallizing in the trigonal CaAl_2Si_2 -type structure. We report zero-field neutron diffraction, temperature T - and magnetic-field H -dependent magnetic susceptibility $\chi(T, H)$, isothermal magnetization $M(T, H)$, heat capacity $C_p(T, H)$, and electrical resistivity $\rho(T, H)$ measurements, together with T -dependent angle-resolved photoemission spectroscopy (ARPES) measurements complemented with first-principles calculations. EuAl_2Ge_2 undergoes second-order A-type antiferromagnetic (AFM) ordering below $T_N = 27.5(5)$ K, with the Eu moments (Eu^{2+} , $S = 7/2$) aligned ferromagnetically in the ab plane while these layers are stacked antiferromagnetically along the c axis. The critical fields at which all moments become parallel to the field are 37.5(5) and 52.5(5) kOe for $H \parallel ab$ and $H \parallel c$, respectively. The $H = 0$ magnetic structure consists of trigonal AFM domains associated with ab -plane magnetic anisotropy and a field-induced reorientation of the Eu spins in the domains is also evident at $T = 2$ K below the critical field $H_{c1} = 2.5(1)$ kOe. The $\rho(T)$ measurements reveal metallic behavior transforming into a slight resistivity increase on cooling towards T_N . A pronounced loss of spin-disorder scattering is observed below T_N . The ARPES results show that EuAl_2Ge_2 is metallic both above and below T_N , and the Fermi surface is anisotropic with two hole pockets at the zone center and one small electron pocket at each M point. In the AFM phase, we directly observe folded bands in ARPES due to the doubling of the magnetic unit cell along the c axis with an enhancement of quasiparticle weight due to the complex change in the coupling between the magnetic moments and itinerant electrons on cooling below T_N . The observed electronic structure is well reproduced by first-principles calculations, which also predict the presence of nontrivial electronic states near the Fermi level in the AFM phase with Z_2 topological numbers 1; (000).

DOI: [10.1103/PhysRevB.107.134439](https://doi.org/10.1103/PhysRevB.107.134439)

I. INTRODUCTION

It is rewarding to study different classes of novel quantum materials having a complex interplay of lattice, spin, and electronic degrees of freedom. These materials can exhibit a plethora of interesting physical properties including superconductivity, heavy fermion behavior, quantum phase transitions, complex magnetic order, magnetic frustration, valence fluctuations, and nontrivial topological phases. One such family of materials is comprised of Zintl-phase compounds that have gained significant recent interest owing to the complex interplay of magnetic and electronic degrees of freedom. These materials exhibit topological states, proximity between

metal-semimetal-semiconductor-insulator phases, anomalous and topological Hall effects, low-field-induced spin reorientations within antiferromagnetic (AFM) domains, along with large thermoelectricity as recently reported in various compounds [1–10].

Many AM_2X_2 -type Zintl-phase compounds have been investigated, where A is an alkaline or lanthanide element, M is a metallic sp element, and X is an sp -element anion where the A atom occupies the positions in either a planar triangular or square-lattice structure. These materials have recently been reported to exhibit electronic states having nontrivial band topology. These states include a topological insulating state, a Dirac/Weyl-type semimetallic state, or an axion-insulating state, and are attractive candidates for dissipationless electron transport [9,11–17]. It has been experimentally found that when the A site of these compounds is fully or partially occupied by a rare-earth element, the materials show enhanced carrier mobility and carrier concentration compared to those

*Present address: Institute for Quantum Materials and Technologies, Karlsruhe Institute of Technology, D-76021 Karlsruhe, Germany.

with A as an alkaline-earth metal [18,19]; the origin of this behavior is currently unknown.

For example, such magnetic Eu-based compounds are of significant interest due to their complex interplay of magnetism and band topology, as reported for EuIn_2As_2 , EuCd_2As_2 , EuMg_2Bi_2 , and EuSn_2As_2 [4,8,11–14,17,20–24]. The magnetic properties associated with different anisotropy energies could thus also play an important role in tuning the electronic states in these materials associated with magnetic ordering. Although the Eu^{2+} ion with spin $S = 7/2$ and orbital angular momentum $L = 0$ exhibits negligible single-ion anisotropy, the magnetic properties in most of these materials are anisotropic [20,21,23,25–28]. Here, the anisotropy arises from magnetic-dipole and/or anisotropic Ruderman-Kittel-Kasuya-Yosida (RKKY) interactions.

To further investigate the properties of this class of materials, here we report the growth of EuAl_2Ge_2 single crystals with the trigonal CaAl_2Si_2 crystal structure [29] and studies of their magnetic, electronic-transport, and electronic-structure properties. These include zero-field neutron-diffraction measurements of the ordered magnetic structure, temperature T - and magnetic-field H -dependent magnetization $M(H, T)$, heat capacity $C_p(T)$, and electrical-resistivity $\rho(H, T)$ measurements, along with T -dependent angle-resolved photoemission spectroscopy (ARPES) studies of the electronic structure. The experimental electronic structure is mapped by calculating the band structure of EuAl_2Ge_2 using density-functional theory (DFT).

We find that EuAl_2Ge_2 is metallic as revealed by the $\rho(T)$ and ARPES measurements complemented with theoretical band-structure calculations. The neutron-diffraction experiments demonstrate that EuAl_2Ge_2 exhibits A-type AFM order below its Néel temperature $T_N = 27.5(5)$ K. In this magnetic structure the Eu^{2+} moments $\mu = 7\mu_B$ with spectroscopic-splitting factor $g = 2$ and spin $S = 7/2$ are aligned ferromagnetically in each ab -plane layer, where the moments in adjacent layers along the c axis are aligned antiferromagnetically. The C_p data for $H = 0$ exhibit a second-order λ -type peak at T_N . The ARPES results further reveal magnetism-induced band folding and enhancement of the quasiparticle intensity in the magnetic ground state. Splitting of the energy bands is observed even above T_N , possibly related to time-reversal symmetry breaking associated with short-range ferromagnetic (FM) correlations above T_N .

Over the broad field range $0 \leq H \leq 55$ kOe, the $M(H)$ data at $T = 2$ K appear to be linear for both $H \parallel ab$ and $H \parallel c$ with respective critical fields $H_{ab}^c = 37.5$ and $H_c^c = 52.5$ kOe, at which all moments become parallel to the respective field. However, detailed $M(H_{ab}, T = 2$ K) measurements at low fields $H_{ab} \leq H_{c1} = 2.5$ kOe exhibit anomalous positive curvature, whereas for $H_{ab} > H_{c1}$ the data are again linear up to H_{ab}^c . This behavior is quantitatively described by a model where the A-type AFM structure occurs in three trigonal domains in which the Eu moments in each domain are aligned at 120° to each other in $H = 0$. With increasing H_{ab} the moments in each domain reorient to become perpendicular to \mathbf{H}_{ab} until H_{c1} is reached, above with all moments progressively cant towards \mathbf{H}_{ab} until H_{ab}^c is attained.

Experimental and theoretical details are given in Sec. II. The results and discussion of the various measurements and

analyses are presented in Sec. III, and concluding remarks are provided in Sec. IV.

II. EXPERIMENTAL AND THEORETICAL DETAILS

Single crystals of EuAl_2Ge_2 were grown using the self-flux method with starting composition $\text{Eu}:\text{Al}:\text{Ge} = 1:20:2$. The Eu (Ames Laboratory), Al (Alfa Aesar, 99.9995%), and Ge (Alfa Aesar, 99.9999%) were loaded into a 2-mL alumina crucible and sealed in a silica tube under 1/4 atm high-purity argon. The assembly was heated to 1175°C inside a box furnace at a rate of $100^\circ\text{C}/\text{h}$. After holding the temperature for 6 h, the furnace was cooled to 700°C at a rate of $10^\circ\text{C}/\text{h}$. The assembly was then centrifuged to separate the crystals from the molten flux. Hexagonal platelike crystals with typical dimensions $3 \times 3 \times 2$ mm³ were obtained from the growth. The homogeneity and chemical composition of the crystals were confirmed using a JEOL scanning electron microscope (SEM) equipped with an energy-dispersive x-ray spectroscopy (EDS) analyzer. The magnetic measurements were carried out using a Magnetic Properties Measurement System (MPMS) from Quantum Design, in the T range 1.8–300 K and with H up to 5.5 T (1 T $\equiv 10^4$ Oe). The $\chi(T)$ measurements were carried out in zero-field-cooled mode, where the sample was cooled to base temperature without field and the magnetization $M(T)$ was measured on heating after application of a field. For the $M(H)$ isotherm measurements the field was oscillated to zero before each measurement to reduce residual magnetic flux trapped in the superconducting solenoid.

A Physical Properties Measurement System (PPMS, Quantum Design) was used to measure $C_p(T)$ and $\rho(T)$ in the T range 1.8–300 K and H up to 9 T. Four-probe $\rho(T)$ measurements were performed. The measurements were performed on as-grown single crystals. Due to the sensitivity of EuAl_2Ge_2 to the ambient environment leading to a rapid sample decomposition, the crystals were not shaped into resistivity bars with precision geometric-factor control by polishing and cutting. However, the crystals had natural shapes suitable for in-plane resistivity measurements, having a length at least three times larger than the width and thickness. Resistivity measurements were performed along arbitrary directions in the ab plane. In all resistivity measurements the magnetic field was oriented transverse to the current direction. Contacts to the fresh surfaces of the crystals were made by attaching 50- μm -diameter silver wires with In solder and mechanically reinforcing the contact with DuPont 4929N silver paint [30]. The contact resistance was typically in the Ω range. After application of the contacts was complete, the samples were covered with Apiezon N grease to provide temporal protection from degradation. For measurements in magnetic fields oriented along the c axis and ab plane, the samples were attached with Apiezon N grease to the sides of a plastic cube. This provides alignment with about $\pm 5^\circ$ accuracy [31].

Single-crystal neutron-diffraction experiments were performed in $H = 0$ using the TRIAX triple-axis spectrometer at the University of Missouri Research Reactor (MURR). An incident neutron beam of energy 30.5 meV was directed at the sample using a pyrolytic graphite (PG) monochromator. A PG analyzer was used to reduce the background. Neutron wavelength harmonics were removed from the beam

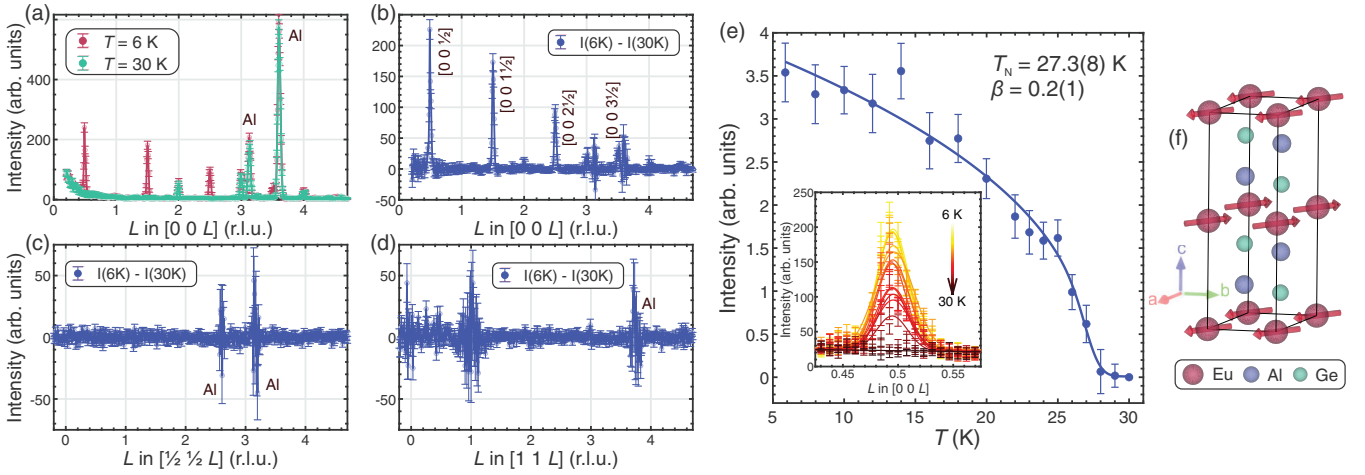


FIG. 1. (a) Zero-field neutron-diffraction pattern along $(00L)$ of single-crystal EuAl_2Ge_2 at 6 and 30 K, as indicated. The aluminum Bragg reflections marked on the figure originate from the sample holder. The magnetic Bragg reflections are obtained by subtracting the diffraction pattern at 30 K from the one at 6 K for (b) $(00L)$, (c) $(\frac{1}{2}\frac{1}{2}L)$, and (d) $(11L)$ scans. The difference pattern in (b) shows clear magnetic peaks at half-integer L up to $L = 3.5$. No such peak is observed in (c), (d) along the $(\frac{1}{2}\frac{1}{2}L)$ and $(11L)$ directions. These observations are consistent with an A-type AFM state, i.e., the $H = 0$ ground state is such that the intraplane moments are ferromagnetically aligned in the ab plane while the moments in adjacent Eu planes along the c axis are aligned antiferromagnetically. Note that structure-factor calculations for this model indicate $(11L)$ at half-integer values of L ; we argue that their absence in (d) is due to the form factor of Eu^{2+} at these relatively large momentum transfers. (e) Integrated intensity as a function of temperature T of the $(00\frac{1}{2})$ magnetic Bragg reflection fitted with a power law to yield $T_N = (27.3 \pm 0.8)$ K and $\beta = 0.21(1)$. (f) Chemical and A-type AFM ground-state structure of EuAl_2Ge_2 . Neutron-diffraction data are insufficient to determine the in-plane moment directions. Therefore, we arbitrarily show the in-plane moments pointing along the next-nearest-neighbor direction.

using PG filters placed before the monochromator and in between the sample and analyzer. Beam divergence was limited using collimators before the monochromator; between the monochromator and sample; sample and analyzer; and analyzer and detector of 60° - 60° - 40° - 40° , respectively. An ≈ 20 mg EuAl_2Ge_2 crystal was mounted on the cold tip of an Advanced Research Systems closed-cycle refrigerator with a base temperature of 4 K. The crystal was aligned in the (HLL) scattering planes. The lattice parameters at base temperature are $a = 4.19(1)$ and $c = 7.27(1)$ Å.

ARPES experiments were performed at the Electron Spectro Microscopy (ESM) 21-ID-1 beamline of the National Synchrotron Light Source II, USA. The beamline is equipped with a Scienta DA30 electron analyzer, with base pressure better than $\sim 1 \times 10^{-11}$ mbar. Prior to the ARPES experiments, samples were cleaved inside an ultrahigh vacuum chamber (UHV) at ~ 9 K. All the measurements were performed using horizontally polarized light. The uncertainty in the temperature values for the ARPES measurements is ± 2 K.

The Vienna *ab initio* simulation package was used for the first-principles calculations [32,33]. For the exchange and correlation energy/potential we used the Perdew-Burke-Ernzerhof (PBE) functional [34]. The projected augmented-wave [35] method was used to represent the core electrons. The cutoff energy for the plane waves was set to 550 eV. A k mesh of $14 \times 14 \times 7$ (AFM phase) and $14 \times 14 \times 12$ in the nonmagnetic (NM) phase was used for the Brillouin-zone integration. Spin-orbit coupling (SOC) was considered in all calculations. The generalized gradient approximation (GGA + U) method [36] was used to treat the correlation effects of $4f$ states in Eu. Furthermore, WANNIER90 was used for the construction of the first-principles tight-binding Hamilto-

nian and constant energy surfaces [37]. The s and p orbitals of Ge and Al and s , p , d , and f orbitals of Eu were used to construct maximally localized Wannier functions. In the case of the NM phase, we treated the f electrons of Eu as core states. The WANNIERTOOLS package was used for the calculation of the Z_2 topological number [38]. For the visualization of the Fermi surfaces, we used FERMISURFER [39].

III. RESULTS AND DISCUSSION

A. Zero-field neutron diffraction

Figure 1(a) shows zero-field neutron-diffraction scans along the $(00L)$ direction in reciprocal-lattice units (r.l.u.) at 6 and 30 K, where reflections at half-integer L values are apparent at $T = 6$ K. For more clarity, Fig. 1(b) shows the difference between these two scans, where within experimental uncertainty, there is no evidence for other reflections associated with a modulated structure along the c axis. We also note that the intensities of the new peaks become weaker at larger L values, roughly following the falloff expected from the magnetic form factor of Eu^{2+} . Similar differences [i.e., $I(6\text{ K}) - I(30\text{ K})$] for scans along $(\frac{1}{2}\frac{1}{2}L)$ and $(11L)$, shown in Figs. 1(c) and 1(d), respectively, do not reveal any magnetic peaks.

Qualitatively, these emerging Bragg reflections indicate a doubling of the unit cell along the c axis. These qualitative observations unequivocally establish that these reflections are associated with A-type AFM ordering with propagation vector $\vec{\tau} = (0, 0, \frac{1}{2})$, consisting of layers of moments aligned ferromagnetically in the ab plane, with moments in adjacent planes along the c axis aligned antiferromagnetically.

The proposed A-type AFM structure is shown in Fig. 1(f), where adjacent nearest-neighbor FM layers along the c axis are rotated by 180° with respect to each other. The direction of the FM moment within an Eu layer cannot be determined from neutron diffraction alone. Using published values, we obtain good agreement with lattice parameters; however, the peak intensities differ significantly from the calculated values due to strong absorption effects by Eu, which are not accounted for in our calculations.

Nevertheless, we are able to confirm the A-type magnetic structure and obtain an estimate for the Eu ordered magnetic moment $\mu = g\langle S \rangle \mu_B = (6.5 \pm 1) \mu_B$ at $T = 6$ K by calculating the magnetic and chemical structure factors, where S is the spin magnetic quantum number, g is the spectroscopic-splitting factor, and μ_B is the Bohr magneton. We note that the large uncertainty in the evaluation of the ordered magnetic moment is mainly due to strong-absorption effects which were not accounted for. Within the error, the fitted value of μ agrees with the expected value $\mu = 7 \mu_B/\text{Eu}$ using $g = 2$ and $S = 7/2$.

Figure 1(e) shows the integrated intensity of the $(00\frac{1}{2})$ magnetic peak as a function of temperature where we use a weighted power-law function by a Gaussian distribution of T_N ,

$$I_{(00\frac{1}{2})}(T) = C|1 - T/T_N|^{2\beta} \propto \mu^2, \quad (1)$$

yielding $T_N = (27.3 \pm 0.8)$ K and $\beta = 0.21 \pm 0.01$. The T_N is in good agreement with the value $T_N = (27.5 \pm 0.5)$ K obtained from the $\chi(T)$ and $C_p(T)$ measurements below.

B. Magnetic susceptibility

The inverse molar magnetic susceptibility $\chi^{-1}(T)$ data measured under an applied field $H = 1$ kOe for both $H \parallel ab$ and $H \parallel c$ are shown in Figs. 2(a) and 2(b), respectively. The data for $T \geq 50$ K for both field directions were fitted by the modified Curie-Weiss law

$$\chi_\alpha(T) = \chi_0 + \frac{C_\alpha}{T - \theta_{\text{pw}}} \quad (\alpha = ab, c), \quad (2)$$

where χ_0 is the temperature-independent contribution, C_α is the Curie constant, and θ_{pw} is the paramagnetic Weiss temperature. The molar Curie constant C_α is given by

$$C_\alpha = \frac{N_A g_\alpha^2 S(S+1) \mu_B^2}{3k_B} = \frac{N_A \mu_{\text{eff},\alpha}^2}{3k_B}, \quad (3a)$$

where N_A is Avogadro's number and the effective magnetic moment is given by

$$\mu_{\text{eff},\alpha} = g_\alpha \sqrt{S(S+1)} \mu_B. \quad (3b)$$

The fits of the $\chi_\alpha^{-1}(T)$ data by Eq. (2) are depicted in Figs. 2(a) and 2(b) for $H \parallel ab$ and $H \parallel c$, respectively, and the fitted parameters are listed in Table I. The effective moments are close to the value $7.94 \mu_B/\text{Eu}$ expected for Eu^{2+} spins with $S = 7/2$ and $g = 2$. The positive values of the Weiss temperatures θ_{pw} are consistent with the A-type AFM order revealed by the above zero-field neutron-diffraction measurements, where the in-plane FM interactions between the Eu spins are dominant over the interplane AFM interactions.

The T dependences of the magnetic susceptibilities χ of EuAl_2Ge_2 measured in $H = 0.1$ kOe for the in-plane

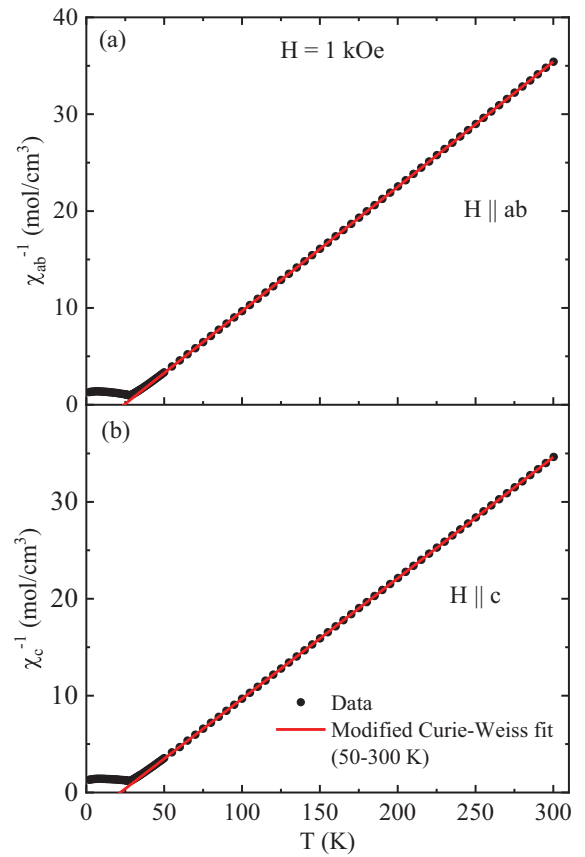


FIG. 2. Inverse magnetic susceptibility as a function of temperature $\chi^{-1}(T)$ measured for $H = 1$ kOe, when (a) $H \parallel ab$ and (b) $H \parallel c$.

($H \parallel ab$) and out-of-plane ($H \parallel c$) field directions are shown in Fig. 3(a). A sharp AFM transition is observed at $T_N = 27.5(5)$ K, which is the same as reported earlier for polycrystalline EuAl_2Ge_2 [40]. The increasing anisotropy between χ_{ab} and χ_c on cooling toward T_N likely arises from FM correlations in the ab plane that increase at T_N is approached from above, since the strongest interactions are within the ab -plane layers that give rise to the observed A-type AFM structure below T_N discussed above.

The $\chi_J(T)$ data above T_N for Heisenberg interactions in the absence of anisotropy are obtained as the average

$$\chi_J(T \geq T_N) = \frac{1}{3}[2\chi_{ab}(T) + \chi_c(T)], \quad (4)$$

TABLE I. Parameters obtained from fits of the data in Figs. 2(a) and 2(b) by Eq. (2). The listed parameters are the T -independent contribution to the magnetic susceptibility χ_0 , Curie constant per mol C_α in $\alpha = ab, c$ directions, effective moment per Eu $\mu_{\text{eff}}(\mu_B/\text{Eu}) \approx \sqrt{8C}$, and Weiss temperature θ_{pw} obtained from the $\chi^{-1}(T)$ vs T data for $H = 1$ kOe.

Field direction	χ_0 ($10^{-4} \frac{\text{cm}^3}{\text{mol}}$)	C_α ($\frac{\text{cm}^3 \text{K}}{\text{mol}}$)	$\mu_{\text{eff},\alpha}$ (μ_B/Eu)	θ_{pw} (K)
$H \parallel ab$	-2.6(3)	7.86(1)	7.93(1)	24.26(7)
$H \parallel c$	-1.9(3)	7.99(1)	7.99(1)	21.86(7)

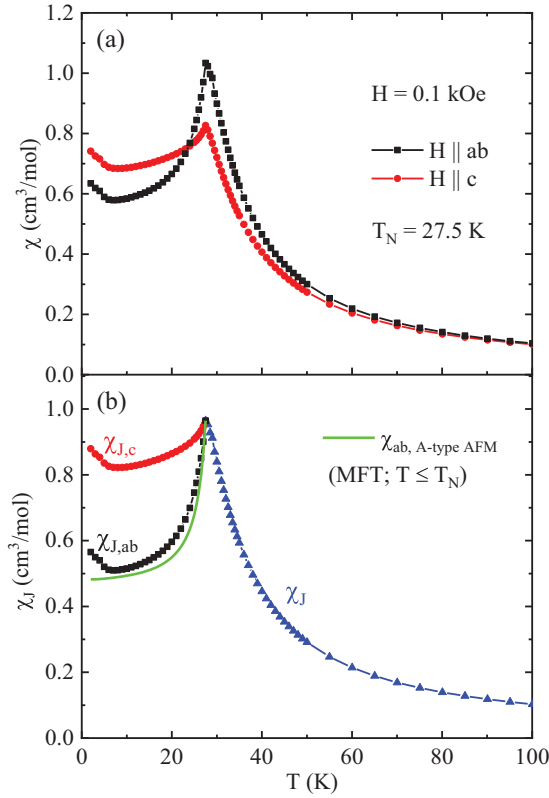


FIG. 3. (a) Temperature dependence of the magnetic susceptibilities measured for $H = 0.1$ kOe with $H \parallel ab$ (black squares) and $H \parallel c$ (red circles). The upturns in the $\chi_{ab}(T)$ and $\chi_c(T)$ data below ~ 5 K may be associated with an additional magnetic ordering of unknown type. (b) Spherically-averaged Heisenberg magnetic susceptibility $\chi_J(T)$ in the NM state with $T \geq T_N$ obtained using Eq. (4) (solid blue triangles). The blue curve connects the data points. The $\chi_{ab}(T)$ and $\chi_c(T)$ data in (a) for $T \leq T_N$ are respectively shifted vertically to match the values at T_N to the value $\chi_J(T = T_N) = 0.96$ cm³/mol. The $\chi_{J,ab}(T \leq T_N)$ for A-type AFM order predicted by Eqs. (5) for $kd = \pi$ rad and $f = \theta_{p,ave}/T_N = 0.853$ is shown as the green curve. For A-type ordering with the moments aligned in the ab plane, one theoretically expects $\chi_{J,ab}(0 \text{ K})/\chi_J(T_N) = 1/2$, close to the observed value.

which is plotted in Fig. 3(b). Then the data at $T \leq T_N$ are shifted vertically until they match the $\chi_J(T \geq T_N)$ data at T_N as shown.

The $\chi_{J,ab}$ data strongly decrease on cooling from T_N to $T \sim 5$ K, whereas the out-of-plane susceptibility $\chi_{J,c}$ is less dependent on the temperature, signifying that the ab plane is the easy plane. This observation is in good agreement with the neutron-diffraction results revealing the A-type nature of the magnetic ground state with the moments aligned in the ab plane. However, below ~ 5 K, both $\chi_{J,c}$ and $\chi_{J,ab}$ increase sharply, indicating the occurrence of an additional magnetic transition of unknown nature at $T \sim 5$ K. Our neutron-diffraction measurements could not examine the additional transition as their low- T limit was 6 K.

Here, we utilize the molecular field theory (MFT) [41,42] for c -axis helical antiferromagnets with the moments aligned in the ab plane with c -axis propagation vector k and interlayer spacing d for which kd is the turn angle between moments in

adjacent layers. The in-plane magnetic susceptibility $\chi_{J,ab}(T)$ associated with Heisenberg spins and spin interactions J for $T \leq T_N$ and no anisotropy can be written as

$$\frac{\chi_{J,ab}(T \leq T_N)}{\chi_J(T_N)} = \frac{(1 + \tau^* + 2f + 4B^*)(1 - f)/2}{(\tau^* + B^*)(1 + B^*) - (f + B^*)^2}, \quad (5a)$$

where

$$f = \theta_{p,ave}/T_N, \quad (5b)$$

$$B^* = 2(1 - f) \cos(kd)[1 + \cos(kd)] - f, \quad (5c)$$

$$t = \frac{T}{T_N}, \quad \tau^*(t) = \frac{(S + 1)t}{3B'_S(y_0)}, \quad y_0 = \frac{3\bar{\mu}_0}{(S + 1)t}, \quad (5d)$$

the ordered moment versus T in $H = 0$ is denoted by μ_0 , the reduced ordered moment $\bar{\mu}_0 = \mu_0/\mu_{\text{sat}}$ with $\mu_{\text{sat}} = gS\mu_B = 7\mu_B$ here is determined by numerically solving the self-consistency equation

$$\bar{\mu}_0 = B_S(y_0), \quad (5e)$$

$B'_S(y_0) = [dB_S(y)/dy]|_{y=y_0}$, and the Brillouin function $B_S(y)$ is

$$B_S(y) = \frac{1}{2S} \left\{ (2S + 1) \coth \left[(2S + 1) \frac{y}{2} \right] - \coth \left(\frac{y}{2} \right) \right\}. \quad (5f)$$

Using the value of f calculated from the values of $\theta_{p,ave}$ and T_N from Table I, the calculated $\chi_{J,ab}(T)$ for $T \leq T_N$ is

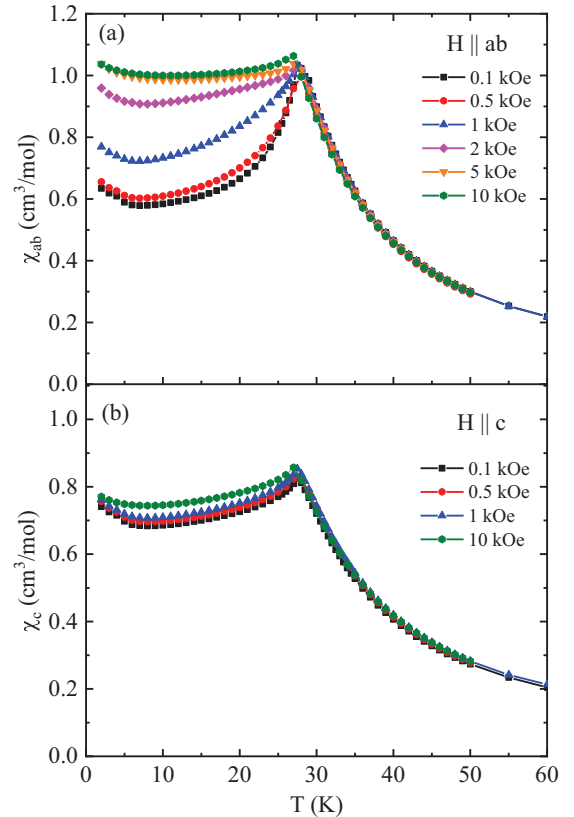


FIG. 4. Magnetic susceptibility $\chi_\alpha(T)$, $\alpha = ab, c$, at different applied magnetic fields for (a) $H \parallel ab$ and (b) $H \parallel c$. Although $\chi_c(T)$ is weakly dependent on H for $T \leq T_N$, $\chi_{ab}(T)$ is strongly H dependent up to $H = 5$ kOe.

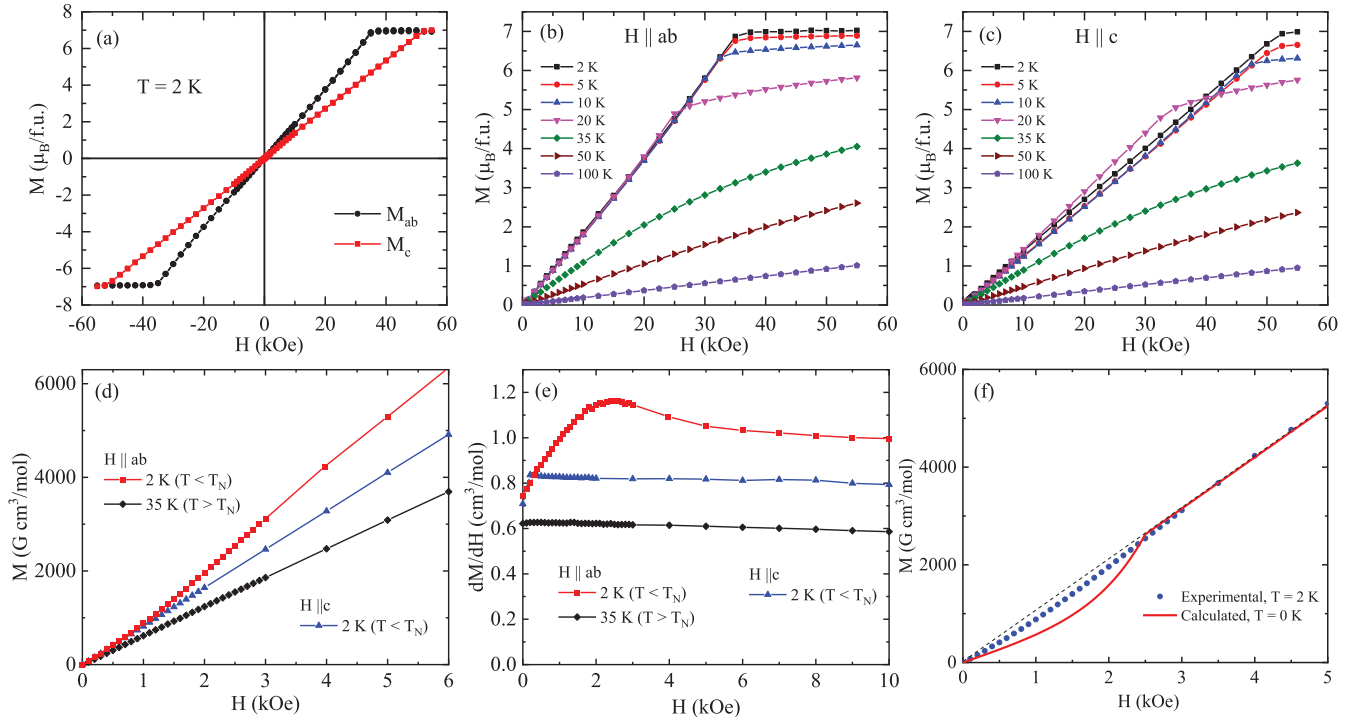


FIG. 5. (a) Magnetic field dependence of isothermal magnetization $M(H)$ in the hysteresis mode for $-5.5 \text{ T} \leq H \leq 5.5 \text{ T}$ measured at $T = 2 \text{ K}$ for both $H \parallel ab$ and $H \parallel c$. $M(H)$ behavior measured at different temperatures for (b) $H \parallel ab$ and (c) $H \parallel c$. (d) Low-field $M(H)$ data showing nonlinearity in the $M_{ab}(H)$ behavior for $T < T_N$, whereas $M_c(H)$ is linear down to the lowest measured temperature 2 K. This nonlinearity is clearly reflected in the dM/dH data shown in (e). (f) The experimental magnetization $M_{ab}(H)$ at $T = 2 \text{ K}$ along with the theoretical prediction for $T = 0 \text{ K}$ with $H_{c1} \approx 2.5 \text{ kOe}$. The dashed line is the guide to the eye of the high-field extrapolated linear behavior. The $M_{ab}(H)$ data exhibit positive curvature for $H < H_{c1}$ as predicted by our theory, but the origin of the quantitative difference between experiment and theory is not clear at present.

shown by the green curve in Fig. 3(b). As seen in the figure, the calculated curve deviates somewhat from the experimental $\chi_{J,ab}(T)$ data, likely due to the additional higher- T magnetic precursor contributions of the anticipated low- T order below 5 K. According to the MFT [41,42], at $T = 0$ we have

$$\frac{\chi_{J,ab}(T = 0)}{\chi_{J,ab}(T_N)} = \frac{1}{2[1 + 2 \cos(kd) + 2 \cos^2(kd)]}. \quad (6)$$

Thus, for an A-type AFM, where the turn angle between adjacent ab -plane FM layers is $kd \rightarrow 180^\circ$, one expects $\chi_{J,ab}(T = 0)/\chi_{J,ab}(T_N) \rightarrow 1/2$, close to the value in Fig. 3(b).

The $\chi(T)$ measured at several applied magnetic fields H are shown in Figs. 4(a) and 4(b) for $H \parallel ab$ and $H \parallel c$, respectively. Interestingly, although the out-of-plane magnetic susceptibility χ_c remains almost independent of H for $H \leq 10 \text{ kOe}$, the in-plane susceptibility χ_{ab} changes significantly with H for $T < T_N$ and H up to 5 kOe. Similar behavior was also observed for the trigonal A-type AFM compounds EuMg_2Bi_2 , EuMg_2Sb_2 , EuSn_2As_2 , and tetragonal EuGa_4 with the moments aligned in the ab plane [10,20,23,43]. We have argued that the A-type ground state spin structure of these materials consist of threefold (for trigonal) or fourfold (for tetragonal) AFM domains associated with in-plane magnetic anisotropy. As Eu^{2+} moments with $L = 0$ provide negligible single-ion anisotropy, magnetic-dipole interaction and other magnetocrystalline anisotropy energies may play a critical role for the formation of AFM domains in these materials. The H -dependent change in the $\chi_{ab}(T)$ behavior is due to

the reorientation of the spins with in-plane field H_{ab} up to a critical field H_{c1} , where all the spins in different domains become perpendicular to the in-plane applied field direction. The spins begin to align along the field direction for $H > H_{c1}$, as expected for a collinear antiferromagnet.

C. Isothermal magnetization versus applied magnetic field measurements

1. Overview

The evolution of the ground-state spin configuration in EuAl_2Ge_2 is further probed by isothermal magnetization versus applied magnetic field $M(H)$ measurements. The $M(H)$ behavior in the hysteresis mode for $-5.5 \text{ T} \leq H \leq 5.5 \text{ T}$ measured at $T = 2 \text{ K}$ is shown in Fig. 5(a). No magnetic hysteresis is observed for fields applied either in the ab plane or along the c axis. Figures 5(b) and 5(c) show the $M(H)$ behavior measured at different temperatures for $H \parallel ab$ (M_{ab}) and $H \parallel c$ (M_c), respectively, for our full field range 0–55 kOe. Here, both M_{ab} and M_c appear to increase linearly with H and saturate above the respective critical field $H_{ab}^c = 37.5(5) \text{ kOe}$ and $H_c^c = 52.5(5) \text{ kOe}$ with a saturation moment $\mu_{\text{sat}} = 7.0(5)\mu_B/\text{Eu}$ at $T = 2 \text{ K}$. The measured μ_{sat} value agrees with $\mu_{\text{sat}} = gS\mu_B = 7\mu_B/\text{Eu}$ expected for Eu^{+2} ions with spectroscopic-splitting factor $g = 2$ and spin $S = 7/2$.

The significant difference between the critical-field values for the two field directions indicates the presence of a considerable magnetic anisotropy in the system with ab -plane

ordering preferred over c -axis ordering in the A-type AFM structure, as also observed in the magnetic susceptibility behavior in Fig. 4. Figures 5(b) and 5(c) show that the H^c values decrease with an increase in the temperature for $T < T_N$ as expected. The $M(H)$ data measured at $T = 50$ K, greater than $T_N = 27.5$ K, are also nonlinear for both the field directions, suggesting the presence of short-range dynamic magnetic correlations in EuAl_2Ge_2 above T_N .

2. Low-field $M_{ab}(H)$ data

The $M_{ab}(H)$ data at $T = 2$ K $\ll T_N = 27.5$ K in Fig. 5(a) measured over our maximum field range below T_N appear to increase linearly up to $H_{ab}^c = 37.5(5)$ kOe above which they saturate. However, a careful study at low fields revealed that $M_{ab}(H)$ at $T = 2$ K exhibits positive curvature at $H \lesssim 2.5$ kOe as shown in Fig. 5(d). The positive curvature is more clearly reflected in the dM_{ab}/dH vs H at $T = 2$ K plotted in Fig. 5(e) that exhibits a broad peak at $H_{c1} = 2.5(1)$ kOe. On the other hand, no nonlinearity is observed in the $M_{ab}(H)$ data at $T > T_N$ or in the $M_c(H)$ data at any temperature. A similar behavior of $M_{ab}(H)$ was observed by us at $T \approx 2$ K, far below the respective T_N for other Eu-based trigonal compounds EuMg_2Bi_2 and EuMg_2Sb_2 containing triangular Eu layers, as well as for the tetragonal compound EuGa_4 containing square-lattice Eu layers [10,21,23,28,43], where each compound exhibits A-type AFM order with the moments aligned in the ab plane as in EuAl_2Ge_2 .

3. Theoretical modeling of the low-field $M_{ab}(H)$ data

Overview. In order to model the nonlinear low-field $M_{ab}(H)$ data at $T \ll T_N$ for EuMg_2Bi_2 , EuMg_2Sb_2 , and EuGa_4 , we previously proposed that the A-type AFM ground state of each contains threefold or fourfold A-type AFM domains of moments for the trigonal and tetragonal spin systems, respectively. In the trigonal case, the three domains are associated with a weak ab -plane magnetic anisotropy energy

$$E_{\text{anis}} = K_3 \sin(3\phi), \quad (7)$$

with minima in the ab -plane azimuthal angle ϕ at $\pi/2$, $5\pi/6$, and $-5\pi/6$ rad, where K_3 is the anisotropy constant. Thus in $H = 0$, the collinear moments in adjacent layers in EuAl_2Ge_2 form three domains with the collinear moments oriented along these three minima as shown in Fig. 6(a).

Upon application of ab -plane magnetic field \mathbf{H}_x , the antiparallel spins in domains B and C initially rotate in a direction to become perpendicular to \mathbf{H} at H_{c1} as shown by the arrows in Fig. 6(a) attached to an angular deviation $\Delta\phi$ for a particular value of the field H_x . This happens because for a collinear antiferromagnet at $T = 0$ K, the magnetic susceptibility parallel to the moments is zero, whereas the susceptibility if the moments are perpendicular to the field $\chi_{\perp} = \chi(T_N)$ according to molecular-field theory (MFT) [42] and hence the lowest energy occurs if the moments are perpendicular to \mathbf{H}_x , as discussed further below. With a sufficiently large $H_x \equiv H_{c1}$, all moments are oriented perpendicular to \mathbf{H}_x apart from a small canting $\lesssim 1^\circ$ towards \mathbf{H}_x that is responsible for the measured magnetization at this field. As discussed quantitatively below, the positive curvature in $M_{ab}(H)$ for $H_x < H_{c1}$ as seen in Fig. 5(f) arises from this magnetic-field-induced

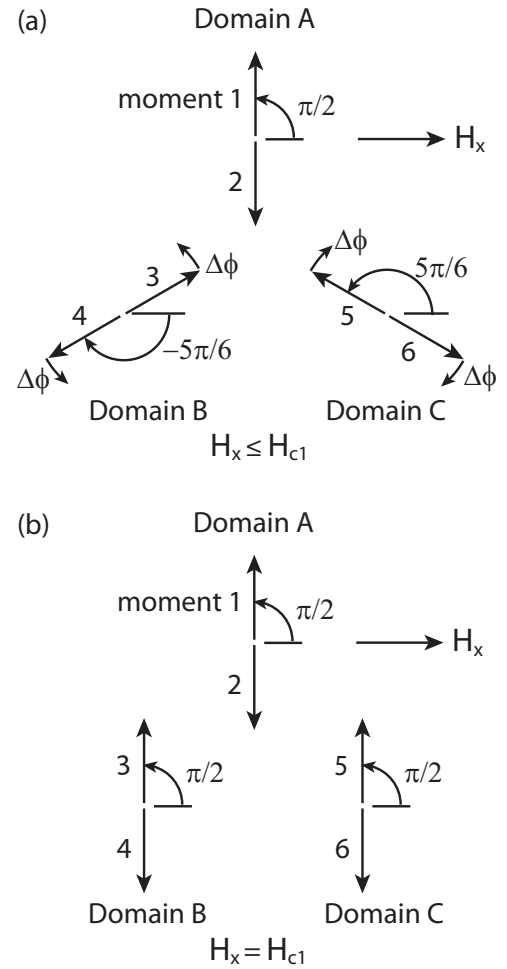


FIG. 6. (a) Reorientation of the Eu magnetic moments in the three trigonal ab -plane antiferromagnetic domains in a small ab -plane magnetic field $H_x < H_{c1}$. Here, the two oppositely-directed arrows in each domain represent the moment orientations in adjacent layers of the A-type AFM structure in small fields. The arrows indicate the direction and increment $\Delta\phi$ of rotation of the moments in domains B and C towards the vertical orientation, perpendicular to the applied field \mathbf{H}_x . The moments in each domain remain antiparallel to each other for $H_x < H_{c1}$ apart from a small canting ($\lesssim 1^\circ$) towards the magnetic field direction that gives rise to the measured magnetization in this field range. (b) Orientation of the moments at the critical field $H_x = H_{c1}$ where all moments are perpendicular to \mathbf{H}_x except for the small canting towards \mathbf{H}_x . At higher fields, all moments cant toward \mathbf{H}_x for $H_{c1} < H_x < H_{ab}^c$ until at the critical field H_{ab}^c all moments are aligned ferromagnetically in the direction of \mathbf{H}_x .

reorientation of the moments in domains B and C. At fields larger than H_{c1} , according to MFT [42] $M_{ab}(H)$ increases linearly up to the critical field H_{ab}^c at which all moments are aligned parallel to \mathbf{H}_x and hence the magnetization saturates to the value $7 \mu_B/\text{Eu}$, in agreement with the experimental data in Fig. 5(a).

Calculations. Here, we summarize the development of the model in Ref. [10] for EuMg_2Bi_2 and EuMg_2Sb_2 as applied to EuAl_2Ge_2 . In the small fields $0 \leq H_x \leq H_{c1}$, the angles of the moments in domains A, B, and C in Fig. 6(a) with respect

to the positive x axis are respectively given by

$$\begin{aligned}\phi_A &= \frac{\pi}{2}, \\ \phi_B &= -\frac{5\pi}{6} + \Delta\phi \quad (0 \leq \Delta\phi \leq \pi/3), \\ \phi_C &= -\frac{\pi}{6} - \Delta\phi. \quad (0 \leq \Delta\phi \leq \pi/3).\end{aligned}\quad (8)$$

The anisotropy energy averaged over the moments in the three domains in the field range $0 \leq H_x \leq H_{c1}$ using Eqs. (7) and (8) is

$$E_{\text{anis ave}} = -\frac{K_3}{3} [1 + 2 \cos(3\Delta\phi)]. \quad (9)$$

The magnetic energy in the regime $0 \leq H_x \leq H_{c1}$ is given by

$$E_{\text{mag}} = -\chi_{\perp} H_x^2 \sin^2(\phi), \quad (10a)$$

where $\chi_{\perp} = \chi_J(T_N)$ (see also below) is the ab -plane magnetic susceptibility at $T = 0$ K when all moments are perpendicular to \mathbf{H}_x , i.e., when $\phi = \pi/2$. Summing over the angles of the moments in the three domains in Eq. (8) and dividing by 3 gives the average magnetic energy as

$$E_{\text{mag ave}} = -\frac{\chi_{\perp} H_x^2}{3} \left[1 + 2 \sin^2 \left(\frac{\pi}{6} + \Delta\phi \right) \right]. \quad (10b)$$

The total average energy $E_{\text{ave}} = E_{\text{anis ave}} + E_{\text{mag ave}}$ is given by the sum of Eqs. (9) and (10b). Then normalizing $E_{\text{mag ave}}$ by K_3 gives

$$\begin{aligned}\frac{E_{\text{ave}}}{K_3} &= -\frac{1}{3} \left\{ 1 + 2 \cos(3\Delta\phi) \right. \\ &\quad \left. + \frac{\chi_{\perp}}{K_3} H_x^2 \left[1 + 2 \sin^2 \left(\frac{\pi}{6} + \Delta\phi \right) \right] \right\}.\end{aligned}\quad (11)$$

Minimizing E_{ave}/K_3 with respect to the quantity $\chi_{\perp} H_x^2/K_3$ yields the relationship between $\Delta\phi$ and H_x given by

$$3 \csc \left(\frac{\pi + 6\Delta\phi}{3} \right) \sin(3\Delta\phi) = \frac{\chi_{\perp} H_x^2}{K_3}, \quad (12a)$$

which yields

$$\frac{\chi_{\perp} H_x^2}{K_3} (\Delta\phi = 0) = 0, \quad (12b)$$

$$\frac{\chi_{\perp} H_{c1}^2}{K_3} (\Delta\phi = \pi/3) = 9/2. \quad (12c)$$

Equation (12c) allows the anisotropy constant K_3 in EuAl_2Ge_2 to be calculated from the known values of the molar $\chi_{\perp} = \chi_J(T_N) = 0.96 \text{ cm}^3/\text{mol}$ from Fig. 3(b) and $H_{c1} = 2.5 \text{ kOe}$ according to

$$K_3 = \frac{\chi_{\perp} H_{c1}^2}{(9/2)N_A} = 1.4 \times 10^{-3} \text{ meV/Eu}, \quad (13)$$

where N_A is Avogadro's number. For comparison, $K_3 = 6.5 \times 10^{-5} \text{ meV/Eu}$ in trigonal EuMg_2Bi_2 [10], $K_3 = 1.8 \times 10^{-5} \text{ meV/Eu}$ in trigonal EuMg_2Sb_2 [10], and $K_4 = 1.4 \times 10^{-3} \text{ meV/Eu}$ in tetragonal EuGa_4 [43].

For $0 \leq H_x \leq H_{c1}$, the magnetization M_x of the collinear moments in a domain at $T = 0$ vs H_x only arises from the component of \mathbf{M} perpendicular to the ferromagnetically aligned layers in the A-type AFM structure, because the

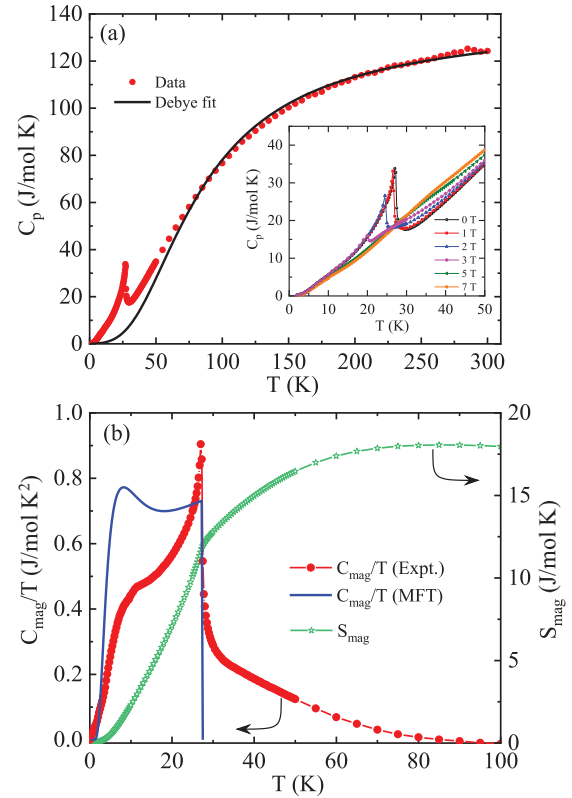


FIG. 7. (a) Temperature dependence of the zero-field $C_p(T)$ for EuAl_2Ge_2 (solid red circles) along with a fit by Eq. (15) (solid black curve). Inset: C_p vs T in magnetic fields H from 0 to 7 T. (b) Plot of C_{mag}/T vs T in $H = 0$ below 100 K (solid red circles, left ordinate) and the corresponding magnetic entropy S_{mag} vs T (right ordinate) calculated from the $C_{\text{mag}}(T)/T$ data using Eq. (17). Also shown as a blue curve is $C_{\text{mag}}(T)/T$ calculated for $S = 7/2$ and $T_N = 27.4$ K using the molecular-field theory prediction in Eq. (16). The magnetic entropy $S_{\text{mag}}(T)$ calculated using Eq. (17) is plotted as the green triangles with the scale on the right ordinate.

parallel component gives no contribution at $T = 0$ K. The normalized magnetization averaged over the three domains using Eqs. (8) is

$$\frac{M_{x \text{ ave}}(\Delta\phi)}{M_x(H_{c1})} = \frac{1}{3} \left[1 + 2 \sin^2 \left(\frac{\pi}{6} + \Delta\phi \right) \right]. \quad (14)$$

Solving for $\Delta\phi(H_x)$ using Eq. (12a) and the known values of K_3 and $M_x(H_{c1})$, a plot of $M_{x \text{ ave}}$ vs H_x over the range $0 \leq H_x \leq H_{c1}$ is shown in Fig. 5(f). At higher fields $H_{c1} \leq H \leq H_{c2}^a$, one has $M(H_x) = \chi_{\perp} H_x$, above which the magnetization saturates, when M_x reaches $M^{\text{sat}} = 7 \mu_B/\text{Eu}$.

D. Heat capacity

The temperature dependence of the zero-field heat capacity $C_p(T)$ of EuAl_2Ge_2 is shown in Fig. 7(a). A clear λ -type peak is observed in the $C_p(T)$ data at $T_N = 27.5$ K, indicating the second-order nature of the AFM transition. The peak position shifts to lower temperature with increasing applied field, as shown in the inset of Fig. 7(a). The $C_p(T)$ tends to saturate at a value of $\approx 124 \text{ J}/(\text{mol K})$, at $T = 300$ K, close to the classical Dulong-Petit high- T limit $3nR = 124.71 \text{ J}/(\text{mol K})$,

where $n = 5$ is the number of atoms per formula unit and R is the molar gas constant.

The molar $C_p(T)$ data were fitted by an electronic contribution γT plus the Debye lattice heat-capacity model according to

$$C_p(T) = \gamma T + nC_{V\text{Debye}}(T),$$

$$C_V(T) = 9R \left(\frac{T}{\Theta_D} \right)^3 \int_0^{\Theta_D/T} \frac{x^4 e^x}{(e^x - 1)^2} dx, \quad (15)$$

where γ is the Sommerfeld electronic specific-heat coefficient and Θ_D is the Debye temperature. An accurate Padé approximant expression for $C_V(T)$ [44] was used for the fit. The fit is shown by the black curve in Fig. 7(a), where $\gamma = 21(2)$ mJ/(mol K²) and $\Theta_D = 332(2)$ K. The γ value is significantly larger than the value of 6(1) mJ/(mol K²) estimated from the theoretical density of states at the Fermi energy $D(E_F)$ value below. The enhancement may be due to electron-electron and/or electron-phonon interactions.

Although the AFM ordering temperature of EuAl_2Ge_2 is $T_N = 27.5$ K, the $C_p(T)$ data exhibit a positive deviation from the fit in Fig. 7(a) for the electronic and lattice contributions up to 80 K, indicating the presence of short-range magnetic correlations up to ~ 80 K. The magnetic contribution $C_{\text{mag}}(T)$ to the heat capacity is obtained by subtracting the electronic and lattice contributions from the measured $C_p(T)$ data using the above fit and is shown as the red symbols in Fig. 7(b). The $C_{\text{mag}}(T)$ remains finite for $T_N < T \lesssim 80$ K evidently due to the presence of short-range dynamic FM correlations in the ab plane, as indicated by the nonlinear $M(H)$ with negative curvature in Fig. 5(b) for $T > T_N$ and the increasing positive deviation of $\chi_{ab}(T)$ from $\chi_c(T)$ with decreasing T in Fig. 3(a).

In Fig. 7(b), we have also shown the theoretical $C_{\text{mag}}(T)/T$ behavior based on the MFT [42] for this system with $S = 7/2$ as the blue line. According to MFT, the molar $C_{\text{mag}}(t)$ is given by

$$C_{\text{mag}}(t) = R \frac{3S\bar{\mu}_0^2(t)}{(S+1)t \left[\frac{(S+1)t}{3B_s(t)} - 1 \right]}, \quad (16)$$

where the symbols are defined in Eqs. (5). The MFT prediction below T_N in Fig. 7(b) does not agree well with the data, although the overall shapes below T_N are similar. In this regard we must keep in mind the presence of the additional transition below ~ 5 K noted above and also the presence of substantial short-range magnetic correlations above T_N .

The temperature dependence of the magnetic entropy $S_{\text{mag}}(T)$ is calculated using the experimental data (red symbols) in Fig. 7(b) and the relation

$$S_{\text{mag}}(T) = \int_0^T \frac{C_{\text{mag}}(T)}{T} dT, \quad (17)$$

as shown by the green symbols with the scale on the right ordinate of Fig. 7(b). The $S_{\text{mag}}(T)$ saturates at $T > 80$ K to a value of ≈ 18 J/(mol K), which is comparable with the theoretical saturation entropy $S_{\text{mag}} = R \ln(2S+1) = 17.29$ J/(mol K) for Eu^{2+} ions with $S = 7/2$. The release of the entropy at temperatures higher than T_N is due to short-range FM correlations in the ab plane above T_N as indicated from the $C_{\text{mag}}(T)/T$ vs

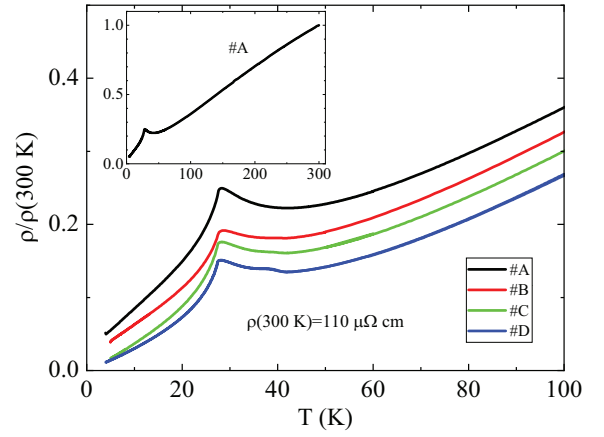


FIG. 8. Temperature T -dependent in-plane electrical resistivity ρ of four EuAl_2Ge_2 crystals in $H = 0$ T below 100 K. The inset shows the full temperature dependence of crystal #A up to room temperature.

T data in Fig. 7(b), as also previously found in other Eu- and Gd-based $S = 7/2$ compounds [20,23,28,45,46].

E. Electrical resistivity

While the general trend of the electrical resistivity ρ in the paramagnetic state of EuAl_2Ge_2 is a metallic decrease on cooling below room temperature as illustrated in the inset of Fig. 8, anomalous behavior is observed on approaching T_N from above as shown in the main panel. In particular, the resistivity develops significant positive curvature from ~ 80 K down to $T_N = 27$ K, corresponding to the development of dynamic short-range magnetic correlations observed in the heat capacity data in Fig. 7. Loss of spin-disorder scattering due to long-range AFM ordering leads to the rapid decrease in the resistivity on cooling below T_N .

The upturn in $\rho(T)$ on cooling below approximately 40 K for sample #A with the best-defined sample geometry is less pronounced in samples #B, #C, and #D. Instead, a small feature appears at ~ 40 K, suggesting the appearance of some form of magnetic correlations. Since these samples were not as perfect in the resistivity-bar aspect ratio as sample #A, it may suggest that the feature stems from contamination of the intraplane resistivity data by the interplane contribution which we did not measure. Further studies are required to address the origin of this feature.

1. Electrical resistivity in magnetic fields $H \parallel c$ axis

In Fig. 9 we show the field-dependent resistivity, measured in magnetic fields parallel to the crystal c axis. Measurements were taken at characteristic temperatures of 60 K (in the paramagnetic state with weak magnetic correlations, cyan line), at 33 K in the correlated paramagnet state (purple line), and at 20 K (green line) and 5 K (black line) in the A-type AFM state. Magnetization versus field measurements at 5 and 20 K in this configuration [Fig. 5(c) above] show a linear increase at low fields and saturation at fields at about 5 T and 3 T, respectively, in very good agreement with the features seen in the $\rho_a(H_c)$ curves. At 20 K the resistivity decreases above

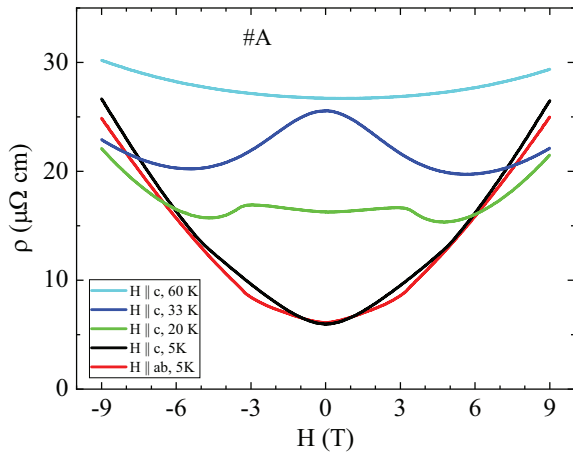


FIG. 9. In-plane resistivity ρ of EuAl_2Ge_2 crystal #A in magnetic fields in the $H \parallel c$ configuration. Measurements were taken at temperatures of 60 K in the paramagnetic state during the initial development of magnetic correlations (cyan line), at 33 K in the more-correlated paramagnetic state (purple line), and at 20 K (green line) and 5 K (black line) in the A-type AFM state. For reference we show data taken in the $H \parallel ab$ configuration at 5 K (red line) for which the critical field is about 3.5 T from Fig. 5(c).

3 T, evidencing the suppression of spin-disorder scattering. At $T = 5$ K, the $\rho_c(H)$ curve shows a slope change at ~ 5 T. For comparison we show resistivity data measured at 5 K in the $H \parallel ab$ configuration, revealing a much clearer feature at the saturation field of ≈ 3.5 T (red curve in Fig. 9).

Note that in the paramagnetic state at 60 K, the resistivity in Fig. 9 increases monotonically with magnetic field, close to the $\rho \sim H^2$ dependence expected for weak-field orbital magnetoresistance [47]. The symmetry of the curve with respect to the sign of the magnetic field suggests a minimal contribution of a spurious Hall effect signal in the resistivity measurements. In the correlated paramagnet state at 33 K the resistivity decreases with field up to a field of ~ 6 T, due to field-induced suppression of spin-disorder scattering. Positive magnetoresistance is restored in the spin-polarized state above 6 T.

2. Electrical resistivity in magnetic field $H \parallel ab$ plane

In Fig. 10 we show the evolution of the temperature-dependent resistivity of EuAl_2Ge_2 with magnetic field applied parallel to the conducting ab plane. This field effectively alters the interplane alignment of the ferromagnetic planes in the type-A antiferromagnet with respect to the field, as discussed in Sec. III C. A strong enough magnetic field of 1 T (red curve) suppresses the pretransition resistivity increase and brings the sharp feature observed in zero field at $T_N = 27$ K to somewhat lower temperatures. With a further field increase to 2 T (green curve), the sharp feature at T_N is smeared and transforms into a broad crossover. It shifts to higher temperatures at $H = 3$ T (blue curve) and becomes hard to distinguish at higher fields of 4 and 6 T, clearly showing the importance of the spin-polarized state for its observation. This behavior is similar to the resistivity minimum above T_N observed in some gadolinium compounds such as GdCuAs_2 [48] and Gd_2CuGe_3

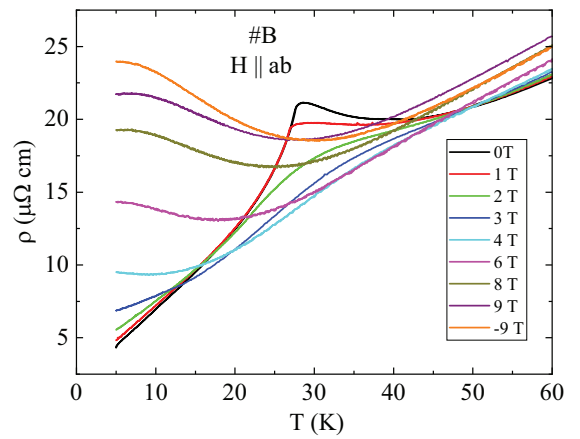


FIG. 10. Temperature-dependent resistivity of EuAl_2Ge_2 in magnetic fields $H \parallel ab$. The sharp feature accompanying long-range AFM ordering at $T_N = 27$ K in zero field moves to a somewhat lower temperature in a field of 1 T (red) and smears and moves to higher temperatures in fields of 2 T (green) and 3 T (blue). Measurements in positive and negative fields of 9 T reveal some contamination of the resistivity signal with the Hall voltage, suggesting a sign change of the Hall effect at around 30 K in the 9 T field.

[49]. It is likely linked to strong magnetic frustration [50,51] leading to a classical spin-liquid state [52].

Figure 11 shows the field-dependent resistivity measured in magnetic fields parallel to the sample ab plane. Measurements were taken at characteristic temperatures of 60 K in the paramagnetic state above magnetic correlation development (blue line), at 33 K in the correlated paramagnet state (green line), and at 20 K (red line) and 5 K (black line) in this configuration [Fig. 5(b)] show positive curvature at the lowest fields [zoomed in Fig. 5(d)], followed by a linear increase and saturation at fields at about 3.5 and 2.5 T, respectively.

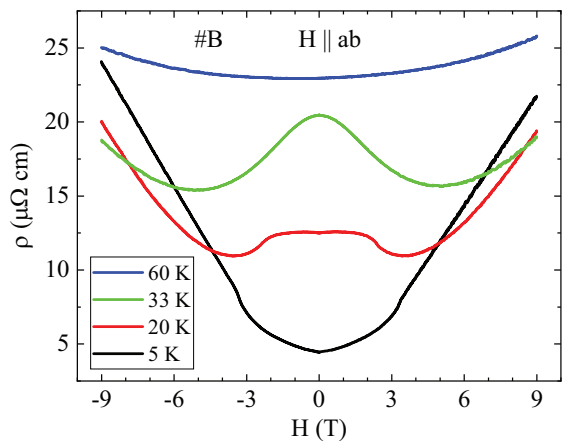


FIG. 11. In-plane resistivity ρ of EuAl_2Ge_2 in magnetic fields with the $H \parallel ab$ configuration. Measurements were taken at characteristic temperatures of 60 K (in the paramagnetic state with weak magnetic correlations, blue line), at 33 K in the correlated paramagnet state (green line), and at 20 K (red line) and 5 K (black line) in the A-type AFM state.

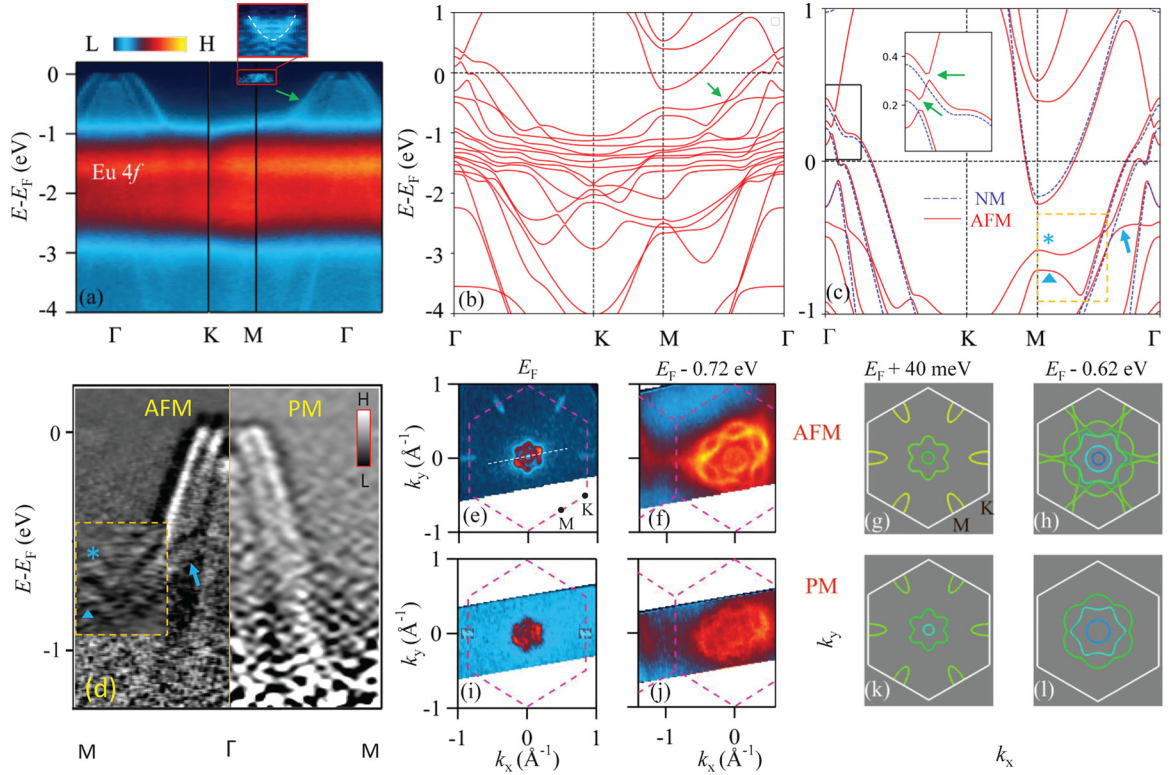


FIG. 12. Electronic structure of EuAl_2Ge_2 . (a) ARPES spectrum of EuAl_2Ge_2 along the Γ -K-M- Γ path measured in the AFM phase (9 K) using $h\nu = 91$ eV ($k_z \sim 0$). The inset shows the zoomed-in spectra of the electron pocket at the M point. The arrow indicates the crossing point of two bands. (b) Theoretical band dispersions including spin-orbit coupling (SOC), Hubbard $U = 5$ eV, and A-type AFM spin configuration using DFT. The arrow indicates the crossing of bands. (c) Theoretical band dispersions in the AFM and NM phases are plotted together. The inset shows zoomed-in spectra around Γ . Band inversion/avoided-crossing features are indicated by the two green arrows in the inset. Compared to the NM phase, a few extra bands appear in the AFM phase and some of them are indicated by an arrow, star, and triangle symbols. (d) Two-dimensional second-derivative of the ARPES spectra along Γ -M for AFM and NM phases. Bands within the dashed box are captured by theoretical calculations in (c). Fermi surface and constant-energy contours for the AFM phase in the experiment [(e), (f)] and theory [(g), (h)] and similarly, for the NM phase (40 K) in the experiment [(i), (j)] and theory [(k), (l)]. Different energy values are used between the experiment and theory as the position of the Fermi level is slightly different between them. The ARPES spectra in Fig. 14 were taken along the cut shown by the white dashed line in (e).

This is in very good agreement with the features seen in $\rho(H)$ curves. At 20 K the resistivity decreases above 2 T, reaches a minimum at 3 T, and increases on further field increase. Note a tiny resistivity increase for the 5 and 20 K curves, presumably related to magnetic-moment rotations as discussed above in Sec. III C.

F. Electronic structure from ARPES measurements and DFT calculations

In order to understand the interplay of magnetism and electronic structure in EuAl_2Ge_2 , ARPES measurements have been performed at different temperatures, with a particular emphasis on the temperature range bridging T_N . The experimentally observed electronic structure was also compared with the theoretical electronic structure by density-functional-theory (DFT)-based calculations.

Figure 12(a) shows the ARPES spectrum of EuAl_2Ge_2 along the Γ -K-M- Γ path, measured in the AFM phase at $T = 9$ K. The spectrum shows two holelike and one electronlike bands crossing the Fermi level E_F at the Γ and M points of the Brillouin zone (BZ), respectively. These holelike bands appear

to cross at -0.5 eV along Γ -M [indicated by the green arrow in Fig. 12(a)], but they are well separated along Γ -K. For better visualization of the electron pocket, a closer view is shown in the inset of Fig. 12(a). Extremely less-dispersive bands with high intensity are observed around -1.5 eV due to the localized Eu-4*f* levels. Most of the experimental features are reasonably well reproduced by DFT calculations, which consider the effect of spin-orbit-coupling (SOC) and a Hubbard $U = 5$ eV to account for the effect of strong localization of the half-filled Eu-4*f* orbitals of EuAl_2Ge_2 in its A-type AFM spin configuration as obtained from our neutron-diffraction measurements [Fig. 12(b)].

In order to identify potential changes in the electronic structure associated with the magnetic transition, the AFM and NM band structures are plotted together in Fig. 12(c). In the AFM phase, several new bands appear compared to the NM phase, due to the doubling of electronic states originating from the doubling of the magnetic unit cell dimension along the c axis. For example, an electronlike band is observed in the AFM phase, just above E_F at the Γ point, whereas it is absent in the NM phase. This electronlike band crosses two holelike bands and causes various band anticrossings, as

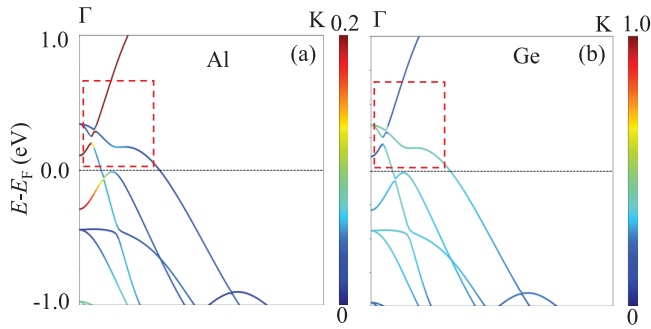


FIG. 13. Atom-projected band structure in the AFM phase of EuAl_2Ge_2 without spin-orbit coupling for the contributions of (a) Al and (b) Ge to the electronic states. Band inversion between the Al and Ge states is observed within the dashed red boxes.

indicated by the arrows in the inset of Fig. 12(c). The band inversion is found to occur between the Al and Ge states, even in the absence of spin-orbit coupling as shown in Fig. 13. Unfortunately, these states are inaccessible by photoemission spectroscopy as they appear above E_F . However, potential changes in the electronic states between the NM and AFM phases are also expected below E_F as indicated in Fig. 12(c) by asterisk and triangle symbols with the dashed box, and arrow, and that should be directly accessible by ARPES. Indeed, we resolve those folded shallow bands in the AFM phase of EuAl_2Ge_2 as indicated in Fig. 12(d), whereas no such states are observed in the NM phase. Generally, folded electronic states appear weaker in photoemission, regardless of whether they are due to magnetism or charge density waves [53–56].

Further, to map the dispersion of the electronic states in the k_x - k_y plane, Fermi-surface (FS) mapping was performed. Figures 12(e) and 12(i) show the FS of EuAl_2Ge_2 for the AFM and NM phases, respectively. In both cases, three Fermi pockets are observed, two at the center of the BZ, and one at the M point. The circular and hexagonal Fermi pockets at the center of the BZ are formed by the inner and outer holelike bands, respectively [Fig. 12(a)], and the elongated oval-shaped Fermi pocket at the M point is the electron pocket. This electron pocket is formed by the bottom of the conduction band that enters inside the Fermi level. The inner Fermi pocket is isotropic whereas the other two are very anisotropic. All these FSs are well reproduced by theoretically computed contours at $E_F + 40$ meV [Figs. 12(g) and 12(k)]. This energy shift was used to better match the shape and sizes of the experimental FS features, suggesting that the sample is slightly electron doped.

The FS features and dispersion of electronic states suggest that EuAl_2Ge_2 is metallic, both in the AFM and NM phases. Further, according to the band structure, folded bands between two consecutive BZs should connect the M point at a deeper energy that cuts the folded bands at the M point. Indeed, we observe this signature both in our ARPES and theoretical simulated constant-energy contours, as shown in Figs. 12(f) and 12(h), respectively. In the NM case, no such intensity is observed at the M point due to the absence of band folding [Figs. 12(j) and 12(i)]. Recently, magnetism-induced band folding and nontrivial band topology were

reported in the Eu-based AFM system EuCd_2As_2 [53,54]. As discussed above, our DFT calculations also predicted inverted band features in the AFM state of EuAl_2Ge_2 near E_F , which is typically observed in materials hosting nontrivial band topology. To correctly verify its nontrivial topological origin, we have calculated the Z_2 topological numbers using the Wilson loop (Wannier charge center) method [37] for the six time-reversal-invariant momentum planes. The obtained Z_2 topological numbers $\nu_0; (\nu_1\nu_2\nu_3) = 1; (000)$ indicate the presence of nontrivial electronic states in this system. Further theoretical studies are needed to determine the exact nature of the “topology” of the system. In particular, to understand the exact nature of the topology of the system, accounting for the magnetic space group is necessary but is not considered in our calculations.

To obtain more insight into the electronic-structure change across the magnetic transition, we have performed high-resolution ARPES measurements close to E_F at various temperatures [Figs. 14(a)–14(c)]. While they exhibit very similar spectral features across the transition, the quasiparticle weight decreases significantly. This can be better visualized in their energy-distribution curves (EDCs) in Fig. 14(d). The temperatures at which the quasiparticle weight drops correlate well with magnetic transition temperatures. This drop in quasiparticle weight in the NM phase is most possibly related to the complex interplay between the orbital and spin degrees of freedom, caused by the change of coupling between magnetic moments and itinerant electrons across magnetic transitions.

Quasiparticle enhancement in magnetically-ordered states has been reported in other magnetic materials due to the decrease of spin fluctuations and changes in the scattering mechanism [57,58]. Further zooming the ARPES spectra in momentum reveals that the individual holelike bands actually split in two. The splitting is better resolved for the outer bands as indicated by the vertical lines in Figs. 14(e) and 14(f). The momentum distribution curves (MDCs) also show clear two-peak structures of the outer band. It is interesting to note that the band splitting survives above T_N .

However, according to the theoretical calculations, all the bands in the AFM and NM phases are twofold degenerate, so no such band splitting is expected. Thus only two holelike bands are expected to cross E_F [Fig. 12(c)]. Generally, band splitting occurs when either time-reversal symmetry T or parity P symmetry is broken. Even though T is broken in the AFM phase, the double degeneracy of the bands is protected by the combination of P , T , and translation (L) symmetries by one unit along the c axis [54]. The observation of band splitting in the NM phase is quite surprising as both the T and P symmetries should be preserved.

On the other hand, based on our magnetic measurements, the persistence of short-range FM correlations above T_N may cause the T symmetry to break in the NM phase, leading to band splitting. In EuCd_2As_2 , an analogous band splitting was reported [53]. The band splitting was explained as resulting from quasistatic and quasi-long-range FM fluctuations experienced by the itinerant electrons. In the AFM phase of EuAl_2Ge_2 , the magnetic moments align ferromagnetically within a basal plane, which results from dominant in-plane FM exchange interactions. Since ARPES is a very surface-

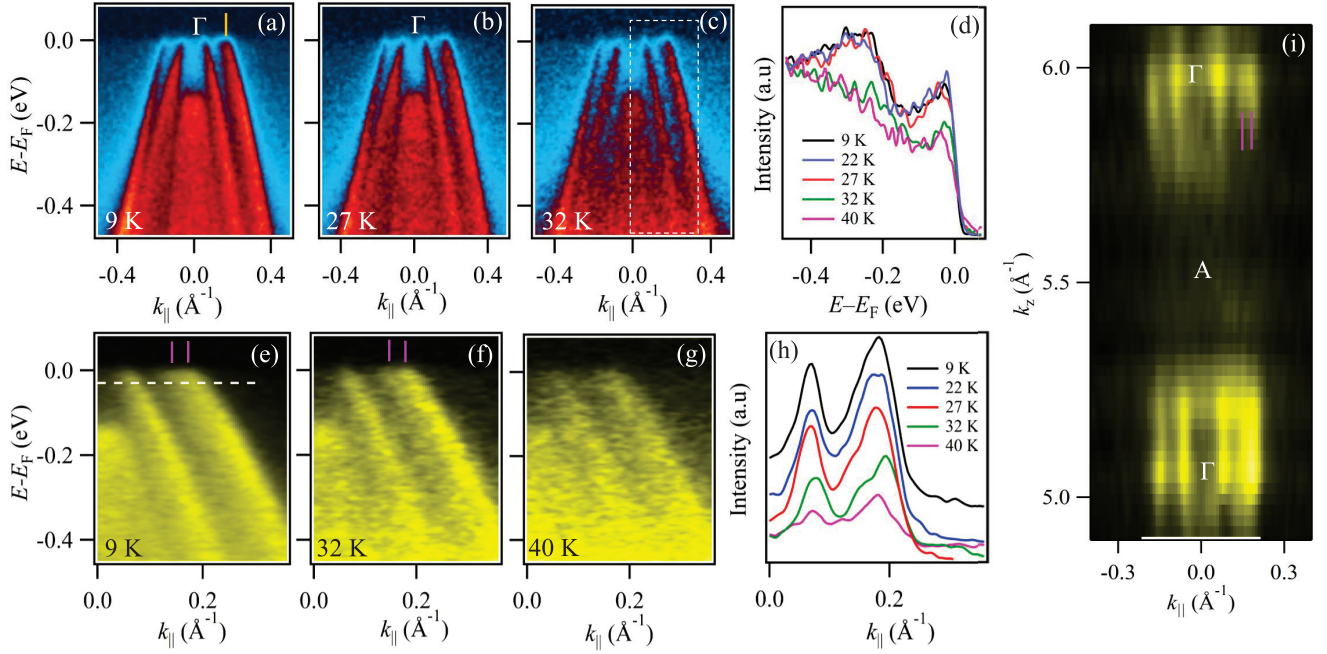


FIG. 14. Electronic structure of EuAl₂Ge₂ across the magnetic transition. (a)–(c) ARPES spectrum around Γ close to E_F along the cut shown by the dashed line in Fig. 12(e) for various temperatures 9, 27, and 32 K, respectively. (d) Temperature dependence of the energy distribution curves (EDCs) at the momentum indicated by a vertical line in (a). (e)–(g) Zoomed view of the ARPES spectra within the region as indicated by a dashed rectangle in (c) for 9, 32, and 40 K, respectively. Vertical red lines indicate the splitting of bands. (h) Momentum distribution curves (MDCs) along the dashed line in (e). The MDC curves were smoothed. (i) The k_z dependence of the electronic states along the dashed line in Fig. 12(e) at $T = 9$ K. The vertical lines indicate splitting of bands.

sensitive technique, these FM interactions may result in the band splitting in the magnetically-ordered state, as observed in Fig. 14(e). We note that the splitting-like feature of electronic states may also appear in ARPES spectra due to the presence of surface states or k_z broadening of electronic states. However, as evident from the k_z dispersion in Fig. 14(i), all the electronic states are predominantly three-dimensional bulk states, ruling out surface states as a possible origin. Furthermore, the observed k_z dispersion suggests that the k_z broadening is unlikely to cause the splitting.

IV. CONCLUDING REMARKS

We find that EuAl₂Ge₂ is a metallic antiferromagnet with nontrivial electronic states in the AFM phase near E_F . The compound exhibits A-type AFM order below $T_N = 27.5(5)$ K with the Eu moments aligned in the ab plane. The anisotropic magnetic properties exhibited by the system, associated with the Eu²⁺ spins, indicate the presence of substantial magnetic-dipole and magnetocrystalline anisotropy. The presence of in-plane magnetic anisotropy results in trigonal threefold AFM domain formation in $H = 0$. The moments in the domains exhibit a field-induced reorientation at $H_{c1} \sim 2.5(1)$ kOe to become perpendicular to the field direction for $T < T_N$. The ab -plane and c -axis critical fields at $T = 2$ K are $H_{ab}^c = 37.5(5)$ kOe and $H_c^c = 52.5(5)$ kOe at which all

moments are polarized along the respective applied-field directions.

The presence of dynamic short-range magnetic correlations within the ab planes is evident above T_N from the zero-field heat capacity and resistivity studies. A slight resistivity increase on cooling before loss of spin-disorder scattering below T_N suggests magnetic correlations which are different from long-range AFM ordering. Similarly, ARPES studies reveal band splitting even above T_N , suggesting a possible breaking of the T symmetry associated with the magnetic correlations above T_N which are therefore identified to be ferromagnetic in nature. The ARPES results further reveal that EuAl₂Ge₂ is metallic with a well-defined Fermi surface. The Fermi surface is formed by the two hole pockets at the zone center (Γ) and electron pockets at each M point. The outer hole pocket and the electron pockets at M are very anisotropic. Overall, the ARPES results show a highly anisotropic three-dimensional electronic structure of EuAl₂Ge₂ that could be responsible for the anisotropic magnetic properties observed in our experiments. In addition to the various dispersive bands, extremely less-dispersive bands are observed around an energy -1.5 eV below the Fermi energy due to the localized Eu-4*f* levels. Various folded bands are also observed in the AFM phase due to the doubling of the unit cell. All these electronic states are modeled well by considering spin-orbit coupling (SOC), $U = 5$ eV, and the A-type ab -plane AFM configuration of the Eu magnetic moments.

ACKNOWLEDGMENTS

The research at Ames National Laboratory was supported by the U.S. Department of Energy, Office of Basic Energy Sciences, Division of Materials Sciences and Engineering. Ames National Laboratory is operated for the U.S. Department of Energy by Iowa State University under Contract No. DE-AC02-07CH11358. The research at Brookhaven National Laboratory was supported by the U.S. Department of Energy, Office of Basic Energy Sciences, Contract No. DE-SC0012704. This work was also supported in part by the Center for Spintronics Research Network, Tohoku University.

- [1] C. Zheng, R. Hoffmann, R. Nesper, and H. G. Von Schnering, Site preferences and bond length differences in CaAl_2Si_2 -type Zintl compounds, *J. Am. Chem. Soc.* **108**, 1876 (1986).
- [2] J. Shuai, J. Mao, S. Song, Q. Zhang, G. Chen, and Z. Ren, Recent progress and future challenges on thermoelectric Zintl materials, *Mater. Today Phys.* **1**, 74 (2017).
- [3] L.-L. Wang, A. Kaminski, P. C. Canfield, and D. D. Johnson, Different topological quantum states in ternary Zintl compounds: BaCaX ($X = \text{Si, Ge, Sn}$ and Pb), *J. Phys. Chem. C* **122**, 705 (2018).
- [4] S. X. M. Riberolles, T. V. Trevisan, B. Kuthanazhi, T. W. Heitmann, F. Ye, D. C. Johnston, S. L. Bud'ko, D. H. Ryan, P. C. Canfield, A. Kreyssig, A. Vishwanath, R. J. McQueeney, L.-L. Wang, P. P. Orth, and B. G. Ueland, Magnetic crystalline-symmetry-protected axion electrodynamics and field-tunable unpinned Dirac cones in EuIn_2As_2 , *Nat. Commun.* **12**, 999 (2021).
- [5] Z. Zhu, M. Li, and J. Li, Topological semimetal to insulator quantum phase transition in the Zintl compounds Ba_2X ($X = \text{Si, Ge}$), *Phys. Rev. B* **94**, 155121 (2016).
- [6] M. O. Ogunbunmi, S. Baranets, A. B. Childs and S. Bobev, The Zintl phases AlIn_2As_2 ($A = \text{Ca, Sr, Ba}$): New topological insulators and thermoelectric material candidates, *Dalton Trans.* **50**, 9173 (2021).
- [7] N. Varnava, T. Berry, T. M. McQueen, and D. Vanderbilt, Engineering magnetic topological insulators in $\text{Eu}_5\text{M}_2\text{X}_6$ Zintl compounds, *Phys. Rev. B* **105**, 235128 (2022).
- [8] J. Yan, Z. Z. Jiang, R. C. Xiao, W. J. Lu, W. H. Song, X. B. Zhu, X. Luo, Y. P. Sun, and M. Yamashita, Field-induced topological Hall effect in antiferromagnetic axion insulator candidate EuIn_2As_2 , *Phys. Rev. Res.* **4**, 013163 (2022).
- [9] A. K. Kundu, T. Roy, S. Pakhira, Z.-B. Wu, M. Tsujikawa, M. Shirai, D. C. Johnston, A. N. Pasupathy, and T. Valla, Topological electronic structure of YbMg_2Bi_2 and CaMg_2Bi_2 , *npj Quantum Mater.* **7**, 67 (2022).
- [10] S. Pakhira, Y. Lee, L. Ke, and D. C. Johnston, Magnetic-field-induced *ab*-plane rotation of the Eu magnetic moments in trigonal EuMg_2Bi_2 and EuMg_2Sb_2 single crystals below their Néel temperatures, *Phys. Rev. B* **106**, 184423 (2022).
- [11] H. Li, S.-Y. Gao, S.-F. Duan, Y.-F. Xu, K.-J. Zhu, S.-J. Tian, J.-C. Gao, W.-H. Fan, Z.-C. Rao, J.-R. Hugang, J.-J. Li, D.-Y. Yan, Z.-T. Liu, W.-L. Liu, Y.-B. Huang, Y.-L. Li, Y. Liu, G.-B. Zhang, P. Zhang, T. Kondo *et al.*, Dirac Surface States in Intrinsic Magnetic Topological Insulators EuSn_2As_2 and $\text{MnBi}_{2n}\text{Te}_{3n+1}$, *Phys. Rev. X* **9**, 041039 (2019).
- [12] N. H. Jo, B. Kuthanazhi, Y. Wu, E. Timmons, T.-H. Kim, L. Zhou, L.-L. Wang, B. G. Ueland, A. Palasyuk, D. H. Ryan, R. J. McQueeney, K. Lee, B. Schruck, A. A. Burkov, R. Prozorov, S. L. Bud'ko, A. Kaminski, and P. C. Canfield, Manipulating magnetism in the topological semimetal EuCd_2As_2 , *Phys. Rev. B* **101**, 140402(R) (2020).
- [13] Y. Xu, Z. Song, Z. Wang, H. Weng, and X. Dai, Higher-Order Topology of the Axion Insulator EuIn_2As_2 , *Phys. Rev. Lett.* **122**, 256402 (2019).
- [14] M. C. Rahn, J.-R. Soh, S. Francoual, L. S. I. Veiga, J. Stempfer, J. Mardegan, D. Y. Yan, Y. F. Guo, Y. G. Shi, and A. T. Boothroyd, Coupling of magnetic order and charge transport in the candidate Dirac semimetal EuCd_2As_2 , *Phys. Rev. B* **97**, 214422 (2018).
- [15] A. K. Kundu, S. Pakhira, T. Roy, T. Yilmaz, M. Tsujikawa, M. Shirai, E. Vescovo, D. C. Johnston, A. N. Pasupathy, and T. Valla, Electronic and magnetic properties of the topological semimetal SmMg_2Bi_2 , *Phys. Rev. B* **106**, 245131 (2022).
- [16] F. Kabir, M. M. Hosen, F. C. Kabeer, A. Aperis, X. Ding, G. Dhakal, K. Dimitri, C. Sims, S. Regmi, L. Persaud, K. Gofryk, P. M. Oppeneer, D. Kaczorowski, and M. Neupane, Observation of multiple Dirac states in a magnetic topological material EuMg_2Bi_2 , [arXiv:1912.08645](https://arxiv.org/abs/1912.08645).
- [17] M. Marshall, I. Pletikosić, M. Yahyavi, H.-J. Tien, T.-R. Chang, H. Cao, and W. Xie, Magnetic and electronic structures of antiferromagnetic topological material candidate EuMg_2Bi_2 , *J. Appl. Phys.* **129**, 035106 (2021).
- [18] A. F. May, M. A. McGuire, D. J. Singh, J. Ma, O. Delaire, A. Huq, W. Cai, and H. Wang, Thermoelectric transport properties of CaMg_2Bi_2 , EuMg_2Bi_2 , and YbMg_2Bi_2 , *Phys. Rev. B* **85**, 035202 (2012).
- [19] E. S. Toberer, A. F. May, B. C. Melot, E. Flage-Larsend, and G. J. Snyder, Electronic structure and transport in thermoelectric compounds AZn_2Sb_2 ($A = \text{Sr, Ca, Yb, Eu}$), *Dalton Trans.* **39**, 1046 (2010).
- [20] S. Pakhira, M. A. Tanatar, and D. C. Johnston, Magnetic, thermal, and electronic-transport properties of EuMg_2Bi_2 single crystals, *Phys. Rev. B* **101**, 214407 (2020).
- [21] S. Pakhira, T. Heitmann, S. X. M. Riberolles, B. G. Ueland, R. J. McQueeney, D. C. Johnston, and D. Vaknin, Zero-field magnetic ground state of EuMg_2Bi_2 , *Phys. Rev. B* **103**, 024408 (2021).
- [22] M. Marshall and W. Xie, Crystal defect doping on antiferromagnetic topological insulator candidate EuMg_2Bi_2 , *J. Phys. Chem. C* **126**, 737 (2022).
- [23] S. Pakhira, M. A. Tanatar, T. Heitmann, D. Vaknin, and D. C. Johnston, A-type antiferromagnetic order and magnetic phase diagram of the trigonal Eu spin-7/2 triangular-lattice compound EuSn_2As_2 , *Phys. Rev. B* **104**, 174427 (2021).
- [24] X. Lv, X. Chen, B. Zhang, P. Jiang, and Z. Zhong, Thickness-Dependent Magnetism and Topological Properties of EuSn_2As_2 , *ACS Appl. Electron. Mater.* **4**, 3212 (2022).
- [25] Z.-C. Wang, E. Been, J. Gaudet, G. M. A. Alqasseri, K. Fruhling, X. Yao, U. Stuhr, Q. Zhu, Z. Ren, Y. Cui, C. Jia, B.

- Moritz, S. Chowdhury, T. Devereaux, and F. Tafti, Anisotropy of the magnetic and transport properties of EuZn_2As_2 , *Phys. Rev. B* **105**, 165122 (2022).
- [26] T. Berry, V. J. Stewart, B. W. Y. Redemann, C. Lygouras, N. Varnava, D. Vanderbilt, and T. M. McQueen, A-type antiferromagnetic order in the Zintl-phase insulator EuZn_2P_2 , *Phys. Rev. B* **106**, 054420 (2022).
- [27] T. Berry, V. J. Stewart, B. W. Y. Redemann, C. Lygouras, N. Varnava, D. Vanderbilt, and T. M. McQueen, Antiferro- and metamagnetism in the $S = 7/2$ hollandite analog EuGa_2Sb_2 , *Phys. Rev. Mater.* **5**, 114401 (2021).
- [28] S. Pakhira, F. Islam, E. O'Leary, M. A. Tanatar, T. Heitmann, R. Prozorov, A. Kaminski, D. Vaknin, and D. C. Johnston, A-type antiferromagnetic order in semiconducting EuMg_2Sb_2 single crystals, *Phys. Rev. B* **106**, 024418 (2022).
- [29] F. Wartenberg, C. Kranenberg, R. Pocha, D. Johrendt, A. Mewis, R.-D. Hoffmann, B. D. Mosel, and R. Pöttgen, New pnictides with the CaAl_2Si_2 type structure and the stability range of this type, *Z. Naturforsch.* **57**, 1270 (2002).
- [30] M. A. Tanatar, A. E. Böhmer, E. I. Timmons, M. Schütt, G. Drachuck, V. Taufour, K. Kothapalli, A. Kreyssig, S. L. Bud'ko, P. C. Canfield, R. M. Fernandes, and R. Prozorov, Origin of the Resistivity Anisotropy in the Nematic Phase of FeSe , *Phys. Rev. Lett.* **117**, 127001 (2016).
- [31] Y. Liu, M. A. Tanatar, V. G. Kogan, H. Kim, T. A. Lograsso, and R. Prozorov, Upper critical field of high-quality single crystals of KFe_2As_2 , *Phys. Rev. B* **87**, 134513 (2013).
- [32] G. Kresse and J. Furthmüller, Efficient iterative schemes for *ab initio* total-energy calculations using a plane-wave basis set, *Phys. Rev. B* **54**, 11169 (1996).
- [33] G. Kresse and D. Joubert, From ultrasoft pseudopotentials to the projector augmented-wave method, *Phys. Rev. B* **59**, 1758 (1999).
- [34] J. P. Perdew, K. Burke, and M. Ernzerhov, Generalized Gradient Approximation Made Simple, *Phys. Rev. Lett.* **77**, 3865 (1996).
- [35] P. E. Blöchl, Projector augmented-wave method, *Phys. Rev. B* **50**, 17953 (1994).
- [36] A. I. Liechtenstein, V. I. Anisimov, and J. Zaanen, Density-functional theory and strong interactions: Orbital ordering in Mott-Hubbard insulators, *Phys. Rev. B* **52**, R5467 (1995).
- [37] A. A. Mostofi, J. R. Yates, G. Pizzi, Y.-S. Lee, I. Souza, D. Vanderbilt, and N. Marzari, An updated version of WANNIER90: A tool for obtaining maximally-localised Wannier functions, *Comput. Phys. Commun.* **185**, 2309 (2014).
- [38] Q. Wu, S. Zhang, H.-F. Song, M. Troyer, and A. A. Soluyanov, WannierTools: An open-source software package for novel topological materials, *Comput. Phys. Commun.* **224**, 405 (2018).
- [39] M. Kawamura, FermiSurfer: Fermi-surface viewer providing multiple representation schemes, *Comput. Phys. Commun.* **239**, 197 (2019).
- [40] C. Kranenberg, D. Johrendt, A. Mewis, R. Pöttgen, G. Kotzyba, C. Rosenhahn, and B. D. Mosel, Structure and properties of the compounds LnAl_2X_2 ($\text{Ln} = \text{Eu}, \text{Yb}$; $\text{X} = \text{Si}, \text{Ge}$), *Solid State Sci.* **2**, 215 (2000).
- [41] D. C. Johnston, Magnetic Susceptibility of Collinear and Non-collinear Heisenberg Antiferromagnets, *Phys. Rev. Lett.* **109**, 077201 (2012).
- [42] D. C. Johnston, Unified molecular field theory for collinear and noncollinear Heisenberg antiferromagnets, *Phys. Rev. B* **91**, 064427 (2015).
- [43] S. Pakhira and D. C. Johnston, Low-field magnetic anomalies in single crystals of the A-type square-lattice antiferromagnet EuGa_4 , *Phys. Rev. B* **107**, 024421 (2023).
- [44] R. J. Goetsch, V. K. Anand, A. Pandey, and D. C. Johnston, Structural, thermal, magnetic, and electronic properties of the $\text{LaNi}_2(\text{Ge}_{1-x}\text{P}_x)_2$ system, *Phys. Rev. B* **85**, 054517 (2012).
- [45] N. S. Sangeetha, S. Pakhira, D. H. Ryan, V. Smetana, A.-V. Mudring, and D. C. Johnston, Magnetic phase transitions in $\text{Eu}(\text{Co}_{1-x}\text{Ni}_x)_2\text{-yAs}_2$ single crystals, *Phys. Rev. Mater.* **4**, 084407 (2020).
- [46] S. Pakhira, C. Mazumdar, R. Ranganathan, S. Giri, and M. Avdeev, Large magnetic cooling power involving frustrated antiferromagnetic spin-glass state in $R_2\text{NiSi}_3$ ($R = \text{Gd}, \text{Er}$), *Phys. Rev. B* **94**, 104414 (2016).
- [47] J. M. Ziman, *Electrons and Phonons: The Theory of Transport Phenomena in Solids* (Oxford University Press, 2001).
- [48] K. Sengupta, S. Rayaprol, E. V. Sampathkumaran, Th. Doert, and J. P. F. Jemetic, Magnetic and transport anomalies in the compounds, RCuAs_2 ($R = \text{Pr}, \text{Nd}, \text{Sm}, \text{G}, \text{Tb}, \text{Dy}, \text{Ho}, \text{and Er}$), *Phys. B: Condens. Matter* **348**, 465 (2004).
- [49] S. Majumdar and E. V. Sampathkumaran, Magnetic behavior of Gd_2CuGe_3 : Electrical resistance minimum above the Néel temperature, *Phys. Rev. B* **61**, 43 (2000).
- [50] T. Kurumaji, T. Nakajima, M. Hirschberger, A. Kikkawa, Y. Yamasaki, H. Sagayama, H. Nakao, Y. Taguchi, T. Arima, and Y. Tokura, Skyrmion lattice with a giant topological Hall effect in a frustrated triangular-lattice magnet, *Science* **365**, 914 (2019).
- [51] Z. Wang, K. Barros, G.-W. Chern, D. L. Maslov, and C. D. Batista, Resistivity Minimum in Highly Frustrated Itinerant Magnets, *Phys. Rev. Lett.* **117**, 206601 (2016).
- [52] Z. Wang and C. D. Batista, Resistivity minimum in diluted metallic magnets, *Phys. Rev. B* **101**, 184432 (2020).
- [53] J.-Z. Ma, S. M. Nie, C. J. Yi, J. Jandke, T. Shang, M. Y. Yao, M. Naamneh, L. Q. Yan, Y. Sun, A. Chikina, V. N. Strocov, M. Medarde, M. Song, Y.-M. Xiong, G. Xu, W. Wulfhekel, J. Mesot, M. Reticcioli, C. Franchini, C. Mudry *et al.*, Spin fluctuation induced Weyl semimetal state in the paramagnetic phase of EuCd_2As_2 , *Sci. Adv.* **5**, eaaw4718 (2019).
- [54] J. Ma, H. Wang, S. Nie, C. Yi, Y. Xu, H. Li, J. Jandke, W. Wulfhekel, Y. Huang, D. West, P. Richard, A. Chikina, V. N. Strocov, J. Mesot, H. Weng, S. Zhang, Y. Shi, T. Qian, M. Shi, and H. Ding, Emergence of Nontrivial Low-Energy Dirac Fermions in Antiferromagnetic EuCd_2As_2 , *Adv. Mater.* **32**, 1907565 (2020).
- [55] M. Schmitt, P. Moras, G. Bihlmayer, R. Cotsakis, M. Vogt, J. Kemmer, A. Belabbes, P. M. Sheverdyeva, A. K. Kundu, C. Carbone, S. Blügel, and M. Bode, Indirect chiral magnetic exchange through Dzyaloshinskii-Moriya-enhanced RKKY interactions in manganese oxide chains on $\text{Ir}(100)$, *Nat. Commun.* **10**, 2610 (2019).
- [56] V. Brouet, W. L. Yang, X. J. Zhou, Z. Hussain, N. Ru, K. Y. Shin, I. R. Fisher, and Z. X. Shen, Fermi Surface Reconstruction in the CDW State of CeTe_3 Observed by Photoemission, *Phys. Rev. Lett.* **93**, 126405 (2004).

- [57] Y. Zhang, F. Chen, C. He, L. X. Yang, B. P. Xie, Y. L. Xie, X. H. Chen, M. Fang, M. Arita, K. Shimada, H. Namatame, M. Taniguchi, J. P. Hu, and D. L. Feng, Strong correlations and spin-density-wave phase induced by a massive spectral weight redistribution in α -Fe_{1.06}Te, *Phys. Rev. B* **82**, 165113 (2010).
- [58] N. H. Jo, Y. Wu, T. V. Trevisan, L.-L. Wang, K. Lee, B. Kuthanazhi, B. Schruck, S. L. Bud'ko, P. C. Canfield, P. P. Orth, and A. Kaminski, Visualizing band selective enhancement of quasiparticle lifetime in a metallic ferromagnet, *Nat. Commun.* **12**, 7169 (2021).